Geochemistry Geophysics Geosystems G3

Article
Volume 13, Number 1
2 May 2012
Q0AC18, doi:10.1029/2011GC003989
ISSN: 1525-2027

Published by AGU and the Geochemical Society

Melting and channelized magmatic flow in chemically heterogeneous, upwelling mantle

S. M. Weatherley and R. F. Katz

Department of Earth Sciences, University of Oxford, South Parks Road, Oxford OX1 3AN, UK (richardk@earth.ox.ac.uk; samw@earth.ox.ac.uk)

[1] Beneath mid-ocean ridges, magma is thought to rise through a network of high porosity channels that form by reactive flow. Partial mantle melts travel rapidly through these channels to the surface, and retain the geochemical signature of their source rock. Global analyses of mid-ocean ridge lavas indicates that the mantle is chemically heterogeneous, but the consequences of this heterogeneity for reactive porous flow remain unclear. Using numerical models of coupled magma/mantle dynamics, we investigate the relationships between mantle heterogeneity, melting, and magmatic channelization. The models are based on conservation mass, momentum, energy, and composition in a system with two phases and two thermodynamic components in local thermodynamic equilibrium. One of these components is more fusible than the other. In this context, we find that heterogeneities enriched in the more fusible component can nucleate magmatic channels. To understand this result we consider an expression for the melting rate derived from the conservation principles. This expression quantifies the relationship of decompression, reactive flow, and thermal diffusion to the melting rate. With it, we assess their relative importance in the ambient mantle, channels, and enriched heterogeneities. In our models, heat diffuses into fertile channels and powers melting, in combination with reactive flow. These results suggest that thermal diffusion influences the dynamics of magmatic channelization.

Components: 12,600 words, 10 figures, 1 table.

Keywords: magmatic channelization; melt migration; melting; mid-ocean ridge.

Index Terms: 1032 Geochemistry: Mid-oceanic ridge processes (3614, 8416); 1037 Geochemistry: Magma genesis and partial melting (3619); 1038 Geochemistry: Mantle processes (3621).

Received 14 December 2011; **Revised** 12 March 2012; **Accepted** 20 March 2012; **Published** 2 May 2012.

Weatherley, S. M., and R. F. Katz (2012), Melting and channelized magmatic flow in chemically heterogeneous, upwelling mantle, *Geochem. Geophys. Geosyst.*, *13*, Q0AC18, doi:10.1029/2011GC003989.

Theme: Geochemical Heterogeneities in Oceanic Island Basalt and Mid-ocean Ridge Basalt Sources: Implications for Melting Processes and Mantle Dynamics

1. Introduction

[2] Partial melting and melt extraction in the mantle beneath mid-ocean ridges are often described as near-fractional processes [*Langmuir et al.*, 1977; *Johnson et al.*, 1990; *Spiegelman and Kenyon*, 1992; *Hart*, 1993; *Iwamori*, 1993; *Kelemen et al.*, 1997; *Spiegleman and Kelemen*, 2003]. In the simplest case of near-fractional melting, small amounts of melt form over a range of pressures and,

without further chemical interaction with the mantle, get transported to the surface and mixed [*Klein and Langmuir*, 1987; *McKenzie and O'Nions*, 1991]. Once at the surface, these melts erupt and preserve, in the oceanic crust, a chemical record of melting, crystallization, and any reactions that they undergo while traveling through the mantle.

[3] Geochemical analysis of the oceanic crust shows that the composition of erupted magmas varies across the globe. Some of the variation is systematic, and depends on properties of the spreading ridge. *Klein and Langmuir* [1987], for example, showed that the geochemistry of mid-ocean ridge basalts varies systematically with axial depth and the proximity of hot spots. But much of the chemical variation is unstructured and depends on the composition of the source rock [e.g., *Wood*, 1979; *Allègre et al.*, 1984; *Ben Othman and Allegre*, 1990; *Salters and Dick*, 2002; *Seyler et al.*, 2011]. Processes subsequent to melting, such as mixing [*Hirschmann and Stolper*, 1996; *Maclennan et al.*, 2003; *Stracke and Bourdon*, 2009], reaction between magma and the ambient mantle rock [*Yaxley and Green*, 1998], and crystal fractionation [*Grove et al.*, 1992] may disguise the geochemical signal of the source rock; yet the isotopic variability of mid-ocean ridge basalts (MORB) is sufficient to prove that the mantle source is compositionally heterogenous. Recently *Shorttle and Maclennan* [2011] found that heterogeneity in the form of more and less fusible peridotite is sufficient to generate the observed chemical variability of Icelandic basalts. They showed that depleted basalts can result from melting of a depleted peridotite (similar to KLB-1 of *Walter* [1998]), while enriched basalts are likely to derive from a peridotite refertilized by up to 40% MORB. *Shorttle and Maclennan* [2011] also presented a bilithologic melting model that, when combined with geochemical observations, indicates that no more than 10% recycled MORB is present in the bulk mantle. This result is in broad agreement with other suggestions that the mantle source comprises small amounts (≈10%) of eclogite or pyroxenite (>90% pyroxene) hosted in the ambient peridotitic mantle [*Wood*, 1979; *Zindler et al.*, 1979; *Langmuir and Bender*, 1984; *Allègre and Turcotte*, 1986; *Prinzhofer et al.*, 1989; *Langmuir et al.*, 1992; *Chabaux and Allègre*, 1994; *Lassiter and Hauri*, 1998; *Phipps Morgan and Morgan*, 1999; *Pertermann and Hirschmann*, 2003; *Stracke et al.*, 2003; *Ito and Mahoney*, 2005; *Stracke et al.*, 2005; *Kokfelt et al.*, 2006; *Prytulak and Elliott*, 2007; *Jackson et al.*, 2008; *Gale et al.*, 2011].

[4] For the geochemical identity of the source rock to be preserved in the erupted magma, melt transport must occur, to a large extent, without chemical re-equilibration or reaction with the ambient mantle. Chemically isolated flow is also required by observations of disequilibrium between MORB-forming magmas and residual mantle peridotites (rocks containing >40% olivine and >10% pyroxene). For example, residual peridotites (harzburgite and lherzolite) are saturated in orthopyroxene, whereas mid-ocean ridge basalts are not. It follows that MORB-forming magmas are undersaturated in orthopyroxene at Moho pressures. But at pressures greater than 8 kbar the same magmas are saturated in orthopyroxene [*O'Hara*, 1965; *Stolper*, 1980]. This pressure-dependent change in saturation indicates that basalt-forming liquids are chemically isolated from the solid, orthopyroxene-bearing mantle at pressures less than 8 kbar.

[5] Uranium series disequilibria measured in oceanic basalts adds the further, challenging, constraint that melt transport in the mantle must be rapid [*Jull et al.*, 2002; *Stracke et al.*, 2006]. To generate the observed disequilibria, magma must be able to flow from its point of genesis to the surface on a timescale similar to the half-life of ^{230}Th (75 kyr) [*Turner and Bourdon*, 2011].

[6] In general, then, global observations of MORBs require that magmatic flow in the mantle is rapid and chemically isolated, and that magma forms by melting of a chemically heterogeneous mantle. What, if any, is the relationship between these two aspects of magmatism? Is chemically isolated magmatic flow a consequence of mantle heterogeneity? Or can this style of melt transport occur independently of chemical heterogeneities in the source region?

[7] One currently popular model for rapid, chemically isolated melt transport invokes reactive porous flow of magma through a network of high porosity channels. This idea grew around field observations of the Oman ophiolite, which is thought to preserve the crust and uppermost mantle from a spreading ridge [*Tilton et al.*, 1981; *Alabaster et al.*, 1982; *Nicolas*, 1989; *Kelemen et al.*, 1997]. The mantle section of the ophiolite contains a suite of anastomosing, tabular-shaped dunites (>90% olivine) [*Kelemen et al.*, 2000]. The dunites replace, rather than intrude, mantle peridotites, and form when magma, migrating by porous flow, dissolves pyroxene out of the ambient peridotite [*Kelemen et al.*, 1995]. In addition, the erupted melts preserved by the ophiolite are in chemical equilibrium

with the dunites. The implication, therefore, is that dunites in the Oman ophiolite represent fossilized conduits, or channels, through which magma was transported to the surface. Similar conclusions have been drawn from recent observations made on unrelated ophiolites in Italy [*Renna and Tribuzio*, 2011].

[8] The reactive infiltration instability [*Chadam et al.*, 1986; *Ortoleva et al.*, 1987] is thought to provide a mathematical description of how magmatic channels form [*Aharonov et al.*, 1995, 1997; *Kelemen et al.*, 1997; *Spiegelman et al.*, 2001; *Spiegleman and Kelemen*, 2003; *Liang and Guo*, 2003; *Hewitt*, 2010; *Liang et al.*, 2010; *Schiemenz et al.*, 2011; *Liang et al.*, 2011; *Hesse et al.*, 2011]. In this instability, a feedback between melt transport and corrosive dissolution causes magmatic flow to organize into a network of high porosity channels. To generate channels, magma rises buoyantly and dissolves pyroxene out of the ambient peridotite. Regions of larger melt flux accommodate greater dissolution, which increases the local permeability and causes magma to be focused to where it is already concentrated. This is the channel-forming instability.

[9] To understand the implications of the reactive infiltration instability for magmatic flow, *Aharonov et al.* [1995] developed a numerical model of reactive melt transport in a column of chemically homogeneous mantle rock. *Aharonov et al.* [1995] based their model on canonical equations for porous flow and compaction [*McKenzie*, 1984] and, to emulate the behavior of orthopyroxene in the mantle, assumed that the solubility of their model rock was greater at shallower depths. Magma that rose through their model domain consequently reacted with, and removed mass from, the solid. Provided that the solubility gradient was great enough, the flow was unstable, and localized into a network of high porosity channels.

[10] Subsequent models of channel formation [*Spiegelman et al.*, 2001; *Spiegleman and Kelemen*, 2003; *Liang et al.*, 2010; *Schiemenz et al.*, 2011; *Liang et al.*, 2011] followed the same approach as *Aharonov et al.* [1995], but considered only magma flow and channelization in a chemically homogenous mantle, although the specific details of each of these studies varies. For example, *Aharonov et al.* [1995], *Spiegelman et al.* [2001], and *Spiegleman and Kelemen* [2003] modified the composition of the mantle with vanishingly small random perturbations and, in addition to *Liang et al.* [2010] and *Schiemenz et al.* [2011], considered the consequences of incongruent melting. To generate channelized flow, *Liang et al.* [2010] and *Schiemenz et al.* [2011] prescribed a sustained perturbation of porosity to a section of the inflow (bottom) boundary. This boundary condition could, to some extent, be interpreted to capture the behavior of the mantle above an anomalously fusible heterogeneity that is melting. But such an interpretation is inconsistent with the compositional variation of the magma that would be associated with the heterogeneous source.

[11] An important shortcoming of most existing numerical investigations of reactive melt transport and channelized flow is that they neglect the energetics of the system [*Aharonov et al.*, 1995; *Spiegelman et al.*, 2001; *Spiegleman and Kelemen*, 2003; *Liang et al.*, 2010; *Schiemenz et al.*, 2011; *Liang et al.*, 2011]. Melting is an inherently thermodynamic process, and models that predict the melting rate without accounting for conservation of energy are inconsistent. Relatively few computational studies consider melting and magmatic flow in a thermodynamically consistent system [*Ribe*, 1985; *Katz*, 2008, 2010; *Hewitt*, 2010; *Katz and Weatherley*, 2012], and of these only *Hewitt* [2010] and *Katz and Weatherley* [2012] investigate channelized flow. These models share the theoretical framework for porous flow and compaction *McKenzie* [1984] as models that don't conserve energy, but use the Enthalpy Method [*Alexiades and Solomon*, 1993] to close a system of equations that includes conservation of energy. This approach assumes local thermodynamic equilibrium and uses a phase diagram to relate bulk composition, enthalpy, and pressure to the phase compositions, temperature and melt fraction. Since reaction of major elements in the mantle is rapid relative to timescales of melt transport, the assumption of thermodynamic equilibrium is not unreasonable.

[12] An interesting result from the energy-conserving studies of *Katz* [2010] and *Hewitt* [2010] is that channels do not form in an upwelling mantle that has a uniform composition prior to melting. This result is contrary to the previous studies that did not account for conservation of energy [*Aharonov et al.*, 1995; *Spiegelman et al.*, 2001; *Spiegleman and Kelemen*, 2003].

[13] What, then, gives rise to magmatic channels? *Hewitt* [2010] showed that channels only form if the melting region is supplied with a sufficient, additional flux of magma. We hypothesize that this additional flux of magma is supplied by partially melting regions of more fusible rock. Provided that these regions are sufficiently fusible, this flux will nucleate

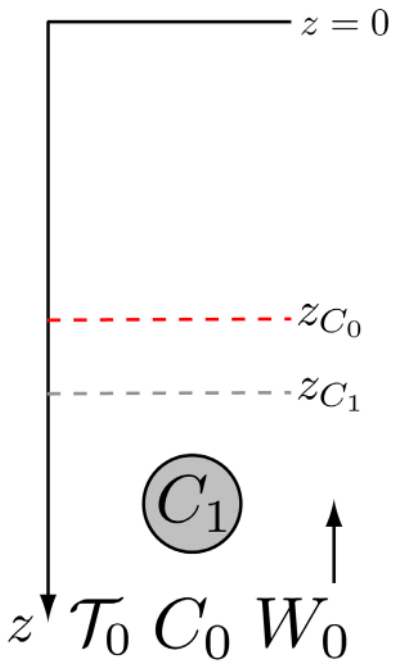

Figure 1. Schematic showing the general setup of our experiments. Solid rock flows into the base of the column at a rate W_0. It has a known potential temperature $\mathcal{T}_0$, and known composition C_0. The initial composition field contains a lithological heterogeneity (grey circle) of composition $C_1 < C_0$ that is enriched in the more fusible chemical component. The ambient mantle begins to melt at a depth z_{C_0}. Since the lithological heterogeneity is more fusible, it begins to melt at the deeper depth of z_{C_1}.

and support high-porosity channels via a mechanism similar to the reactive infiltration instability.

[14] In this paper we examine the effect that chemical heterogeneities have on melting and melt extraction in an upwelling mantle. We use a thermodynamically consistent approach to model the coupled dynamics of magma and solid mantle rock in a thermally and chemically diffusive system. Using suites of numerical experiments, we investigate the effect that a single, isolated heterogeneity has on melting and magma flow, and we vary the physical and chemical characteristics of the heterogeneity between different experiments. Our aim is to elucidate the fundamental dynamics of the system, and so we accept simplifying assumptions such as thermodynamic equilibrium and a simple geometry for the heterogeneity.

[15] In section 2 we outline our numerical model. We describe the results of the model in section 3, and investigate its sensitivity to parameters that are either geologically or theoretically important. We explore the response of the system to the fertility, size, and shape of compositional heterogeneities, the upwelling rate of the mantle, latent heat of fusion and the thermal diffusivity. The results emphasize that the relationships between melting processes, compositional heterogeneities, and magma flow in the mantle are complex, and they underscore the importance of thermal diffusion to magmatic flow and melting in the presence of chemical heterogeneities.

[16] Section 4 presents a derivation of the thermodynamically consistent melting rate, which accounts for thermal and chemical diffusion. The result of the derivation offers a structured framework in which to interpret the results. Using this derivation, we explore how different processes contribute to the melting rate. We conclude section 4 with a discussion of the limitations of our model.

2. Methods

2.1. Domain and Initial Condition

[17] The situation we consider is a two-dimensional column of upwelling rock that contains a compositional heterogeneity (Figure 1). The size and position of the domain are fixed: the top of the domain is aligned with the surface, where the lithostatic pressure is zero, and it extends 120 km into the mantle. Solid rock flows into the base of the domain at a rate W_0. The rock has a known potential temperature $\mathcal{T}$, and has a known composition C_m in a two-component system that forms a solid solution series. One of the components is more fusible than the other. Regions that are enriched in the more fusible component have a lower melting temperature. We refer to these regions equivalently as 'enriched', or 'more fusible'. In contrast, regions that are depleted in the more fusible component melt at a higher temperature. We refer to these regions as being 'depleted', or 'less fusible', although the use of these terms does not necessarily reflect concentrations of trace elements.

[18] The initial condition incorporates a circular chemical anomaly, or enclave, that is enriched in the more fusible component. The form of the anomaly is given by $\mathcal{C}[1/2 + \tanh(r - r_0)/2\lambda]$, where $\mathcal{C}$ gives the degree of enrichment, r_0 is the radius of the heterogeneity and r is the distance of a point from its center, and λ is a parameter that controls the sharpness of the edges of the heterogeneity. At some depth, the ascending mantle begins to melt. Since the enclave is enriched in the more fusible component, and the solidus temperature of the more fusible component is lower at all pressures, the enclave begins to melt at a greater depths than the surrounding, refractory mantle. Above this depth,

the system contains two phases. The rock is modeled as a porous, compactible, solid that behaves as a fluid on geological timescales, and the magma is considered to be a buoyant liquid. At the surface, these interpenetrating fluids flow unrestrictedly out of the domain. The boundary conditions are described in more detail in section A1.

[19] Although our ultimate goal is to gain an insight into processes that might operate beneath a mid-ocean ridge, we do not attempt to model the physical setting of a mid-ocean ridge. At a spreading ridge the motion of the lithosphere introduces a horizontal component of motion into the solid mantle flow field. Since we aim only to understand how mantle heterogeneity influences melt transport in the mantle, we neglect the complicating factors introduced by plate motion. Furthermore, in this paper we will not attempt to infer whether our model can account for geochemistry of erupted magmas. To do so would require similar experiments to be run in a model configured to simulate a mid-ocean ridge. Examples of computations run with boundary conditions corresponding to a mid-ocean ridge are provided in *Katz and Weatherley* [2012].

2.2. Governing Equations

[20] The foundations of the model are conservation statements for mass, momentum, chemical composition, and energy. We provide a comprehensive description of the equations in Appendix A, but discuss important features here.

[21] The set of equations on which the model is founded governs the mechanics and energetics of reactive porous flow in a compacting mantle. They are a reformulated version of the set derived by *McKenzie* [1984], and later by others with minor differences [e.g., *Fowler*, 1985; *Ribe*, 1985; *Scott and Stevenson*, 1986; *Bercovici et al.*, 2001]. In the upwelling column, large scale shear is neglected and the solid velocity $\mathbf{v}_m$ can be written as $\mathbf{v}_m = \nabla U$ [*Spiegelman*, 1993], where U is a velocity potential. This potential is related to the compaction pressure $\mathcal{P}$, which is the difference between the magmatic pressure and the lithostatic pressure. Equations (A1) and (A2) govern $\mathcal{P}$ and U respectively.

[22] Two more equations are needed to account for energy and composition. They are

$$\frac{\partial \mathcal{H}}{\partial t} + \rho c_P \mathcal{T} e^{\frac{\alpha g z}{c_P}} \bar{\mathbf{v}} \cdot \nabla \mathcal{T} = L[\rho \nabla \cdot (1-\phi)\mathbf{v}_m] + k e^{\frac{\alpha g z}{c_P}} \nabla^2 \mathcal{T}, \quad (1)$$

$$\frac{\partial C}{\partial t} + \nabla \cdot \phi \mathbf{v}_f C_f + \nabla \cdot (1-\phi)\mathbf{v}_m C_m = \mathcal{D} \nabla \cdot \phi \nabla C_f. \quad (2)$$

Equation (1) represents the conservation of energy, and is cast as an equation for bulk enthalpy $\mathcal{H}$. In this equation $\mathcal{H} = \rho L \phi + \rho c_P (T - T_0)$ is the volumetric bulk enthalpy, where ρ is density, L is the latent heat of fusion, and ϕ is the porosity, c_P is the specific heat capacity, T is temperature, and T_0 is the melting temperature for material of the reference composition C_0 at zero pressure. $\bar{\mathbf{v}} = \phi \mathbf{v}_f + (1-\phi)\,\mathbf{v}_m$ is the phase averaged velocity, where $\mathbf{v}_f$ is the velocity of the magma, and $\mathbf{v}_m$ is the solid velocity. $\mathcal{T}$ is the potential temperature, α is the coefficient of thermal expansion, k is the thermal conductivity, and z is depth. Equation (1) states that temporal changes in enthalpy arise from advection of latent heat, and advection and diffusion of sensible heat. Equation (2) represents the conservation of composition. Here, $C = \phi C_f + (1-\phi) C_m$ is the bulk composition, where C_f is the composition of the magma, and C_m is the composition of the solid, and $\mathcal{D}$ is the coefficient of chemical diffusion in the magma. This equation states that temporal changes in composition result from advection of composition by the matrix and magma, and by chemical diffusion in the magma. These equations differ from those used by *Hewitt* [2010] by allowing for thermal and chemical diffusion.

[23] To summarize, our model is constructed around four coupled partial differential equations, and we use these equations to solve for $\mathcal{P}$, U, $\mathcal{H}$, and C. These equations, however, depend on the additional variables ϕ, T, C_m, and C_f. We obtain values for ϕ, T, C_m and C_f through closure conditions provided by the Enthalpy Method.

2.3. Idealized Petrological Model

[24] The assumption of local thermodynamic equilibrium requires that the temperature of coexisting rock and magma is equal. We quantify this assumption with an idealized phase diagram shown in Figure 2. To simplify the thermal and chemical dynamics of the system, the solidus and liquidus surfaces are approximated to be linear. They are given by

$$T_S = T_0 + \frac{P_l}{\gamma} + M_S (C_m - C_0), \quad (3)$$

$$T_l = T_0 + \frac{P_l}{\gamma} + M_L (C_f - C_0 + \Delta C), \quad (4)$$

where T_S and T_l are the solidus and liquidus temperatures, P_l is the lithostatic pressure, and γ is the Clapeyron slope, which we take to be constant. M_S and M_L describe the slopes of the solidus and liquidus surfaces respectively. C_0 is the composition

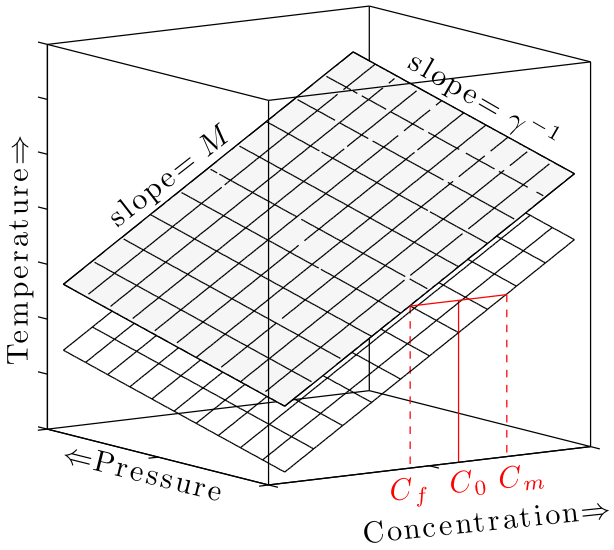

Figure 2. Linearized surfaces for the solidus (lower surface) and liquidus (upper surface). C_0 marks the bulk composition at zero pressure. C_f and C_m show the compositions of coexisting magma and solid rock. The mass fraction of the liquid is given by $(C_0 - C_f)/(C_m - C_f)$.

of the ambient mantle at the onset of melting, ΔC is the compositional difference between rock and magma in equilibrium at the reference temperature T_0. The solidus and liquidus surfaces relate the composition of the magma and matrix to the temperature and lithostatic pressure. *Katz* [2008] describes how equations (3) and (4) are used to solve for ϕ, T, C_f, and C_m.

2.4. Numerical Methods

[25] We discretize the system of governing equations and boundary conditions using a semi-implicit, finite-volume scheme with a grid resolution of 0.5×0.5 km. To assist numerical solution, we split the governing equations into two groups (equations (A1) and (A2) and (A3) and (A4)). At every time-step, each group of equations is solved iteratively using an incomplete LU preconditioned Newton–Krylov method provided by the Portable, Extensible Toolkit for Scientific Computing (PETSc) [*Balay et al.*, 1997, 2009].

[26] To preserve gradients in the system we used a total variation diminishing (TVD) flux limiting advection scheme. *Šrámek et al.* [2010] offer a useful overview of TVD schemes. TVD schemes are conservative and non-oscillatory. Normally, they are second order in space, but near sharp gradients, their order is reduced. The Superbee flux limiter [*Roe*, 1985] is used throughout this paper. Like *Šrámek et al.* [2010], we found it to be the best flux limiter for minimizing dispersion and diffusion.

3. Results

3.1. General Behavior

[27] Figure 3 shows a time series of solutions from a single, representative experiment in terms of different variables. Figures 3a1–3f1 show porosity and Figures 3a2–3f2 show the solid composition. Since we do not map composition onto a real petrological system, we express it as $\Delta T_C = M_S(C_m - C_0)$, which is the difference in solidus temperature due to deviation of the local composition from the reference composition C_0. Figures 3a3–3f3 show the temperature and Figures 3a4–3f4 show the melting rate. To compute Γ we rearrange the conservation of mass equation for the fluid phase (equation (B1)) to give $\Gamma = \rho\left(\frac{\partial \phi}{\partial t} + \nabla \cdot \phi \mathbf{v}_f\right)$. Figures 3a5–3f5 show the the magma speed $|\mathbf{v}_f|$, and Figures 3a6–3f6 show the compaction pressure (equation (A2)). Negative compaction pressures indicate that the matrix is compacting, and that the magmatic pressure is less than the lithostatic pressure.

[28] The experiment in Figure 3 is initialized with a disk of material that is enriched in the more fusible component, with $\Delta T_C = -30°$C. The radius of the disk is 4 km and the initial depth of its center point is 100 km. For all of the other parameters we assign a preferred value, which is listed in Table 1.

[29] The complete time series of results in Figure 3 shows that an enclave of fertile rock, which is embedded into the upwelling mantle, partially melts and supplies the ambient melting region with an additional flux of magma. The additional flux of magma initiates reactive channelization.

[30] The left most column of Figure 3 (Figures 3a1–3a5) shows numerical solutions after a model time of 0.35 Myr. Throughout this paper a model time of zero is equal to the time at which the center point of the anomaly crosses the 100 km depth contour. At this time, the enclave is not partially molten and the ambient melting region is in steady state. Melting of the ambient mantle begins at a depth of 60 km. Above this depth the porosity (Figure 3a1), melting rate (Figure 3a4), magma speed (Figure 3a5), and ΔT_C (Figure 3a2) increase toward the surface; the temperature (Figure 3a3) and magnitude of the compaction pressure decrease (Figure 3a6). These steady state results agree with the one-dimensional

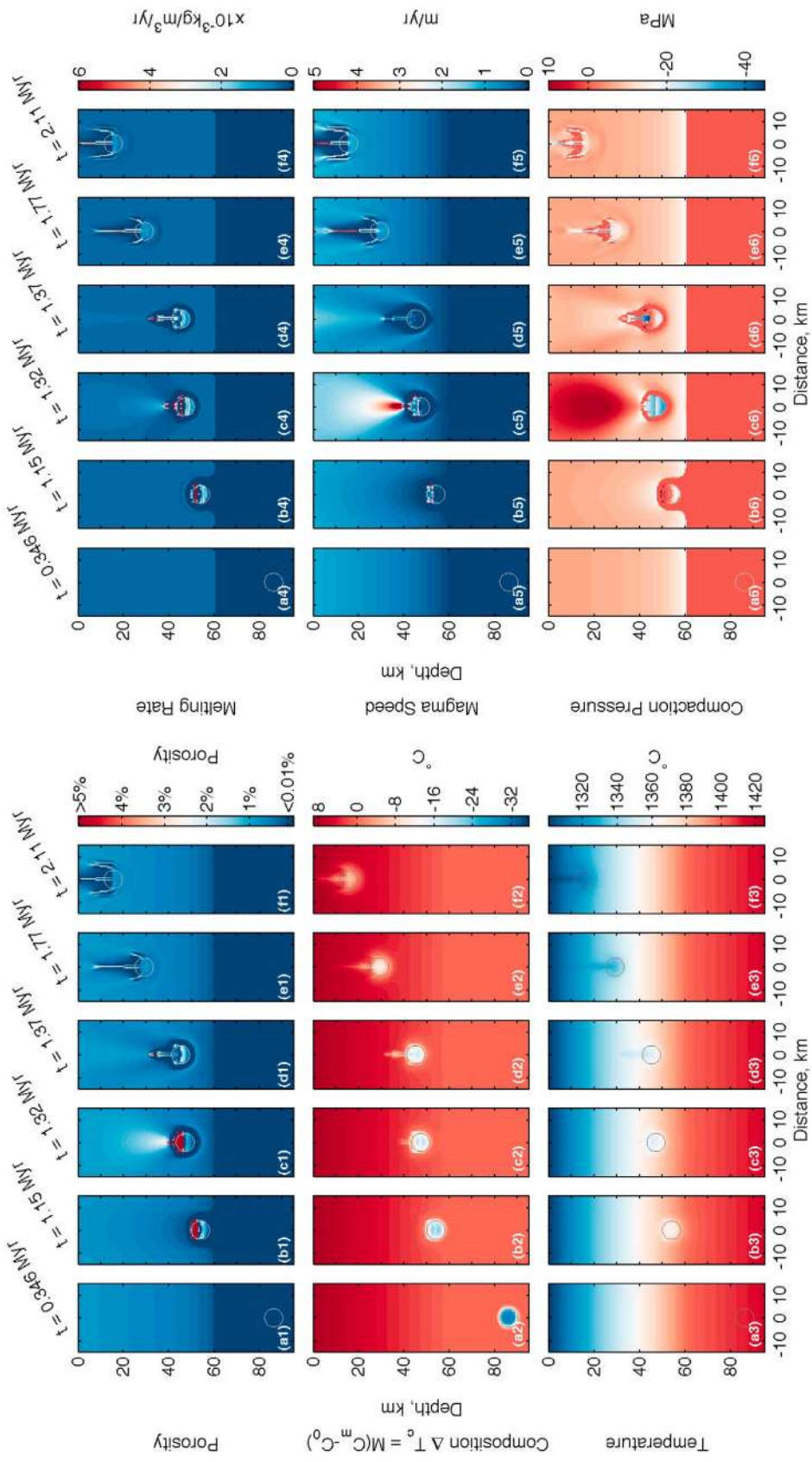

Figure 3. A series of snapshots charting the time evolution of a representative experiment. Columns show the solution at constant timesteps. All parameters take the preferred values listed in Table 1. Yellow circles show what would be the perimeter of the unmolten heterogeneity.

Table 1. List of Parameters and Preferred Values

Symbol	Meaning	Value
R	Enclave radius	4 km
ΔT_C	$M_S(C - C_0)$	-30°C
κ	Thermal diffusivity	1×10^{-6} m/s^2
W_0	Upwelling rate for the matrix	4 cm/yr
L	Latent heat of fusion	4×10^5 J/kg
M_S	Slope $\frac{\partial T}{\partial C}$ of the solidus	400 K
M_L	Slope $\frac{\partial T}{\partial C}$ of the liquidus	400 K
$\mathcal{T}$	Potential temperature	1648 K
T_0	Solidus temperature for reference mantle at 0 kbar	1565 K
C_0	Reference mantle composition	0.85
ΔC	Difference in composition between rock and magma in thermodynamic equilibrium	0.1
ΔT	Temperature scale	$M\Delta C$
ρ	Density	3000 kg/m^3
α	Coefficient of thermal expansion	3×10^{-5} K^{-1}
c_P	Specific heat capacity	1200 J/kg/K
γ^{-1}	Clapeyron slope	60 K/GPa
$\mathcal{D}$	Chemical diffusivity	1×10^{-8} m/s^2
g	Acceleration due to gravity	9.8 m/s^2
k_0	Reference permeability	1×10^{-7} m^2
η_0	Reference shear viscosity	1×10^{19}Pa · s

solutions found by *McKenzie* [1984]; *Ribe* [1985]; *Katz* [2008] and *Hewitt* [2010].

[31] In Figure 3, the second column from the left shows results from our experiment after a model time of 1.15 Myr. Figure 3b1 shows that the enriched enclave has started to melt, and that encasing it is an annulus of unmolten mantle rock. The solidus temperature of rock within the enclave is approximately 20°C cooler than the reference mantle (Figure 3b2). Accordingly, the temperature of rock within the enclave is also lower than the surroundings. Heat diffuses into the enclave and powers melting. But diffusion removes heat from the surrounding mantle and suppresses melting, and so it gives rise to the annulus of subsolidus, impermeable rock that encases the enclave. This cool diffusion halo prevents magma flowing from the enclave into the ambient melting region.

[32] As the enclave and annulus continue to upwell, rock within the annulus melts by decompression, and establishes a magmatic pathway that connects the enclave with the ambient melting region. Figures 3c1–3c5 show the system at an instant after the completion of the pathway. The figures show that magma flowing from the enclave has invaded a balloon-shaped region in the overlying mantle. Within this region the porosity (Figure 3c1) and melting rate (Figure 3c4) are larger than the ambient values. Two effects give rise to the larger porosities and melting rates. First, the fluid pressure of the initial magma that leaves the enclave is greater than the lithostatic pressure, and so $\mathcal{P} > 0$ (Figure 3c6). Thus the infiltrating magma mechanically increases the porosity in the overlying mantle. However, $\mathcal{P}$ remains positive only for a relatively short period of time (approximately 50 kyr, Figure 3). Second, the flux of the infiltrating magma is greater than the ambient upwards flux of magma. Since the infiltrating magma is enriched, it must react with the ambient mantle rock to maintain thermodynamic equilibrium. By this reaction, the melting rate and porosity in the overlying mantle are increased.

[33] Figures 3d1–3d5 show that 50 kyr after the magmatic pathway is established, a channel emerges from the enclave. The channel grows by the same feedback that is fundamental to the reactive infiltration instability: enriched magma flows into the channel, the porosity increases by reaction, and so the channel can accommodate an even greater flux of magma. Within the channel, however, the matrix compacts and works to stabilize the flow, but the rate of porosity generation by melting outstrips the rate of porosity destruction by compaction, and so the channel grows. The channel itself accommodates a higher porosity (Figure 3d1), melting rate (Figure 3d4), and magma speed (Figure 3d5) than the ambient mantle. It is enriched in the more fusible chemical component (Figure 3d2) and, as a consequence, the temperature within the channel is a minimum for a given depth (Figure 3d3). Heat, therefore, diffuses laterally into the channel, cooling the surrounding mantle and preventing it from melting. In this way, thermal diffusion encourages magmatic channelization at the expense of diffuse porous flow.

[34] Over the remainder of the experiment (Figures 3e1–3f5) the channel grows and delivers magma to the surface. Initially, channels grow at a rapid rate, but the growth rate slows with time. Figures 3d2, 3e2, and 3f2 show that the fusibilities of the residual mantle within the enclave and channel gradually decrease with time, but the porosity, magma speed, and melting rate remain significantly larger than the ambient values. The elevated melting rate within the channel is associated with strong compaction (Figure 3e6). Figures 3e1–3f1 show that new channels begin to form on the flanks of the existing channel. The mechanisms that control the location of these channels remain unclear.

[35] One feature of this and subsequent experiments is that the porosity generated within enclaves can

exceed 20%. At porosities greater that 20% the matrix is likely to disaggregate [*McKenzie*, 1984], which violates our assumption of magma flowing through a porous matrix. Our aim, however, is not to fully capture the dynamics of magma flow within enclaves, nor the process of magma leaving the enclave. To do so would widen the scope of our models to include, amongst other processes, brittle fracture [*Nicolas*, 1986] and open fracture channels [*Hewitt and Fowler*, 2009]. Instead, we focus on the dynamics that arise when a partially molten enclave supplements the ambient melting regions with an additional flux of magma. Since the porosity within enclaves drops to reasonable background values immediately after the onset of channelization, we are confident that the large porosities generated within the enclaves do not adversely affect the trajectory of our experiments.

3.2. Thermodynamic Controls

3.2.1. Latent Heat

[36] The latent heat of fusion is an important control on melting, since it couples the rate of melt production to the energetic budget. We explore how L affects melting, and its subsequent influence on channelization, with an ensemble of five experiments (Figure 4). For these experiments we varied L over an order of magnitude between $L = 9 \times 10^4$ J/kg and $L = 9 \times 10^5$ J/kg. Experimental work by *Kojitani and Akaogi* [1997] suggests that a reasonable value for the latent heat of fusion of mantle peridotite is 5×10^5 J/kg. All remaining parameters take their values from Table 1. In Figure 4 and each subsequent figure, the center column shows results from an experiment run with our preferred parameter values from Table 1.

[37] Figures 4a1–4e1 show the results from the experiments in terms of porosity after a model time of 600 kyr. In each experiment, magma from the enriched enclave has not yet infiltrated the ambient melting region. Figures 4b1–4e1, which are taken from experiments where $L \geq 1.5 \times 10^5$ J/kg, show that the style of magmatic flow in the ambient melting region prior to the addition of melt from the more fusible enclave is stable, diffuse porous flow (Figures 4b1–4e1). When $L < 1.5 \times 10^5$ J/kg, however, magmatic flow in the ambient melting regime is unstable; channels form independently of mantle heterogeneity (Figure 4a1). In this simulation, channels grow downward over time, and stop growing at a depth of approximately 30 km. Figures 4a2–4e3 show results from the same suite of experiments in terms of porosity and ΔT_C at the later model time of 1.65 Myr. They show that when L is large, the fertility of enclaves decreases more slowly (Figures 4a3–4e3), and channels grow more slowly (Figures 4a2–4e2).

[38] Analysis of the results shows that the melting rate varies inversely with the latent heat. When L is small, enclaves melt more rapidly and supply a greater flux of enriched magma to their network of channels. Consequently, channels grow more rapidly when L is small. The inverse relationship between L and the melting rate also manifests itself in the properties of the ambient melting region. For example, when L is small and the melting rate is high, the porosity of the ambient mantle is large. The large porosity accommodates a greater upwards flux of magma. In the experiment where $L = 9 \times 10^4$ J/kg the upwards flux of magma is sufficient to generate channels without requiring and additional flux of magma from a more fusible heterogeneity.

3.2.2. Thermal Diffusion

[39] To determine how the thermal diffusivity affects the dynamics of the system, we vary the thermal diffusivity between 10^{-7} m^2/s and 10^{-5} m^2/s within a suite of five different simulations. Every other parameter uses the default value given in Table 1.

[40] Figure 5 shows results to these experiments after a model time of 0.91 Myr in terms of porosity (Figures 5a1–5e1) and ΔT_C (Figures 5a2–5e2). For each experiment the same amount of time has elapsed, yet Figures 5a2–5e2 show that the enclaves in the most diffusive experiments are the least fertile (Figures 5a2–5e2). This implies that melting rates are higher in more thermally diffusive experiments. Consequently, partial melting of enclaves in more diffusive systems can supply their network of channels with magma at a faster rate. In such systems, channels tend to grow more quickly, have a higher porosity, and accommodate faster melting rates and magma speeds.

[41] A cool diffusion-halo also forms around magmatic channels. Figure 5 shows that the permeability of the rock within the diffusion-halo varies with the enrichment of the rock and magma within a channel. When rock within a channel is more fertile, and therefore cooler, the surrounding mantle is less permeable. This is because a greater amount of heat diffuses into more fertile channels to maintain thermodynamic equilibrium. Since thermal diffusion toward channels removes heat from the

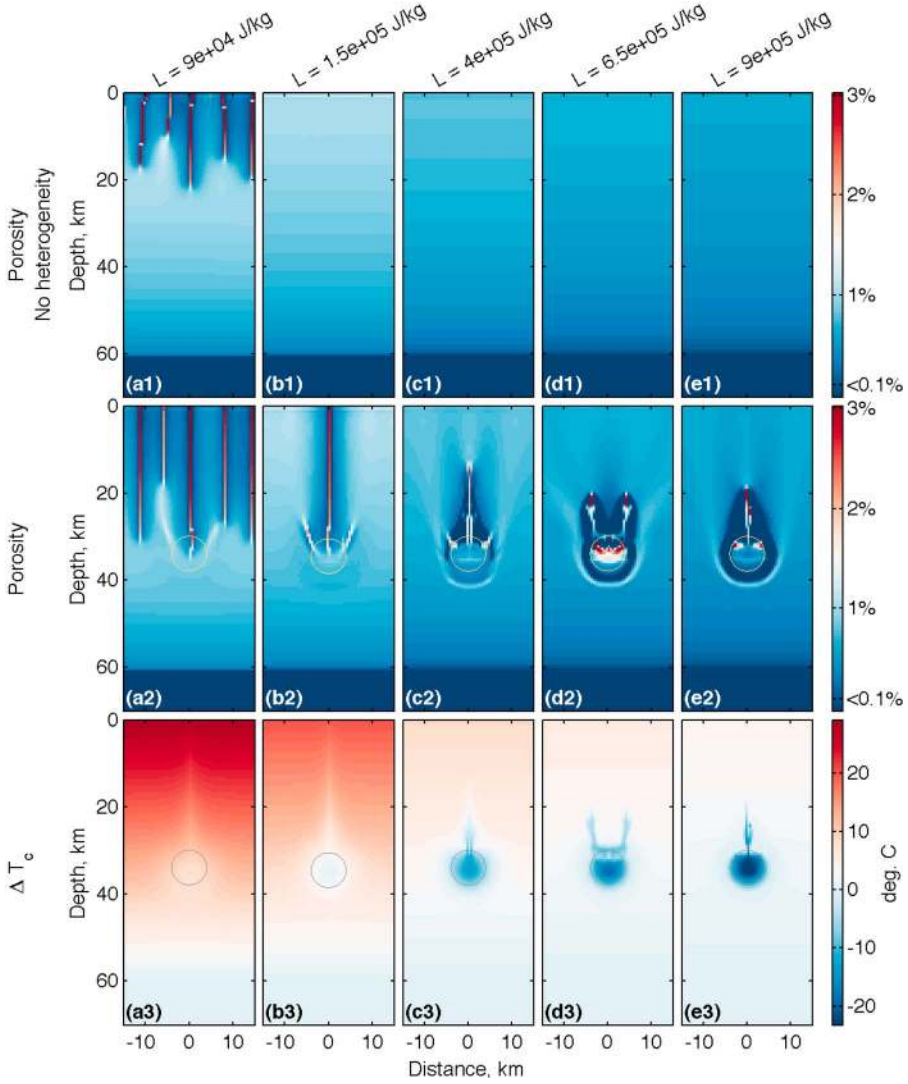

Figure 4. Solutions to a suite of experiments for which the latent heat of fusion L is varied. All other parameters are assigned the values listed in Table 1. (a1–e1) These panels show solutions, in terms of porosity for experiments that are not initialized with an enriched heterogeneity. (a2–e2 and a3–e3) These panels show solutions from the similar experiments that were initialized with an enriched heterogeneity. These panels also show the solutions after a model time of 1.65 Myr in terms of porosity and ΔT_C respectively. Circles show what would be the perimeter of the unmolten heterogeneity.

surrounding rock, material within the diffusion-halo has less enthalpy available for melting, and its porosity is lower.

3.3. Geophysical Controls

3.3.1. Size

[42] We explore the effect that the enclave's size has on channelization using a suite of five different experiments (Figure 6). For these experiments the initial radius of the enriched enclave ranges between 2 km and 6 km. This range agrees with *Helffrich* [2002], who estimated the characteristic size of mantle heterogeneity to be ca. 8 km. All other parameters take the values listed in Table 1. Figure 6 shows results from these experiments after a model time of 1.65 Myr. The top row shows the porosity, and the bottom row shows the composition, expressed in terms of ΔT_C. At the time of the snapshots, the larger enclaves remain more fusible and support channels that have a longer total length.

[43] Figure 6 shows that the larger enclaves, which initially contained a larger mass of the more fusible component, remain more fertile after the same model time has elapsed. It is difficult to assess, from the results presented in this paper, how the

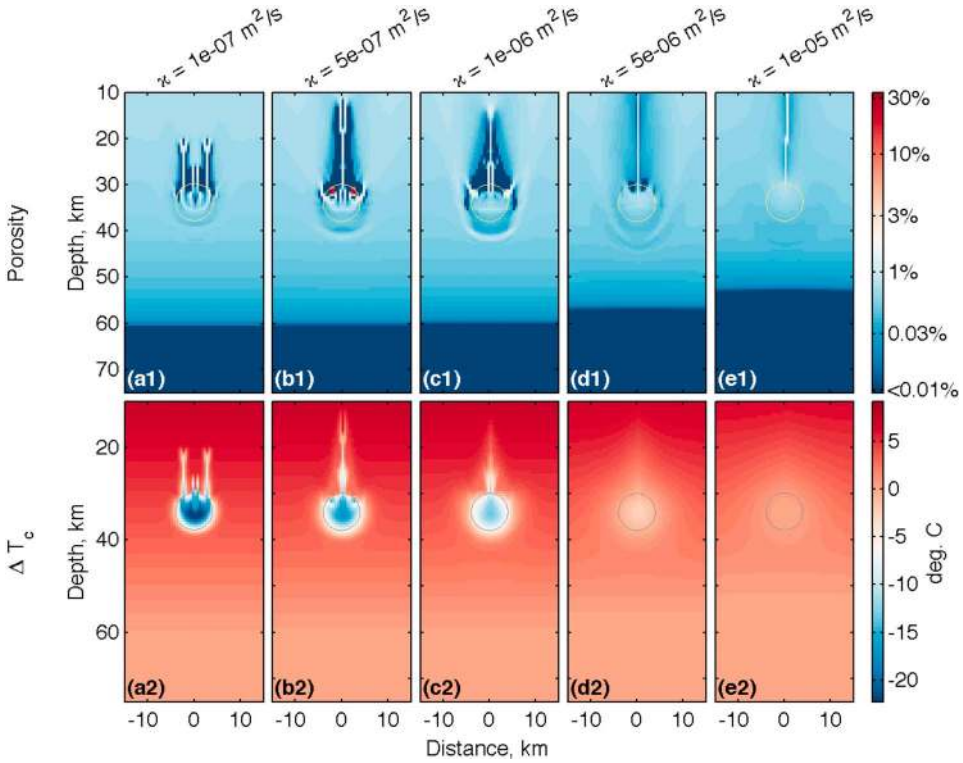

Figure 5. Solutions to a suite of five different experiments for which the thermal diffusivity is varied. All other parameters are assigned the default values given in Table 1. The figures show results from the experiments in terms of (a1–e1) porosity and (a2–e2) ΔT_C after a model time of 0.91 Myr. Panels referenced by the same letter are taken from the same experiment. Circles show what would be the perimeter of the unmolten enclave.

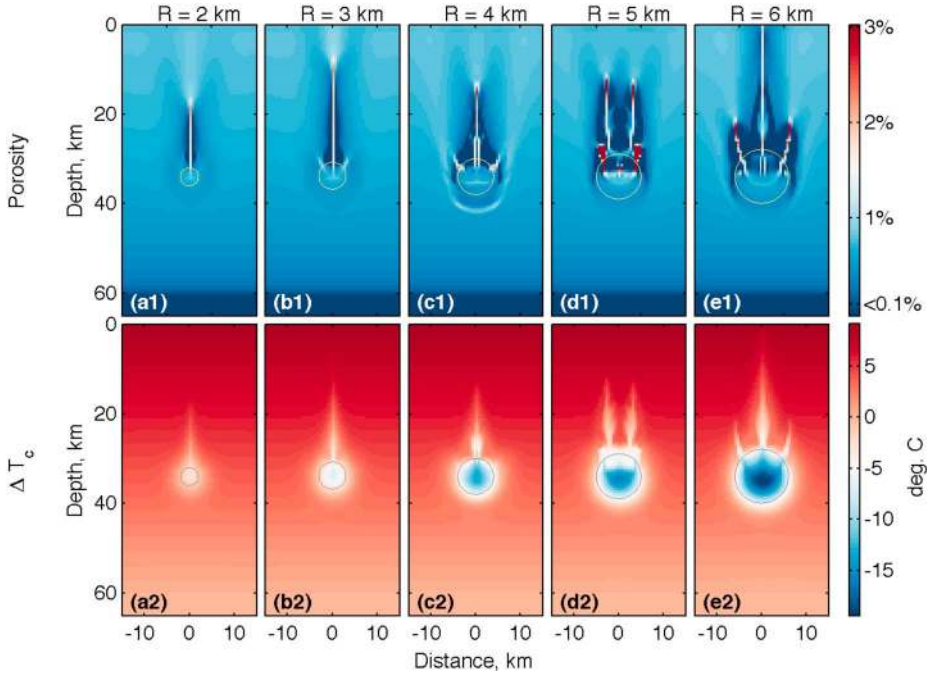

Figure 6. Solutions from a suite of five different experiments at t = 1.65 Myr for which the radius R is varied. All other parameters use the default values given in Table 1. Snapshots referenced by the same letter are taken from the same experiment. (a1–e1) These panels show the solutions in terms of porosity. (a2–e2) These panels show ΔT_C. Circles show the perimeter of what would be the unmolten enclave.

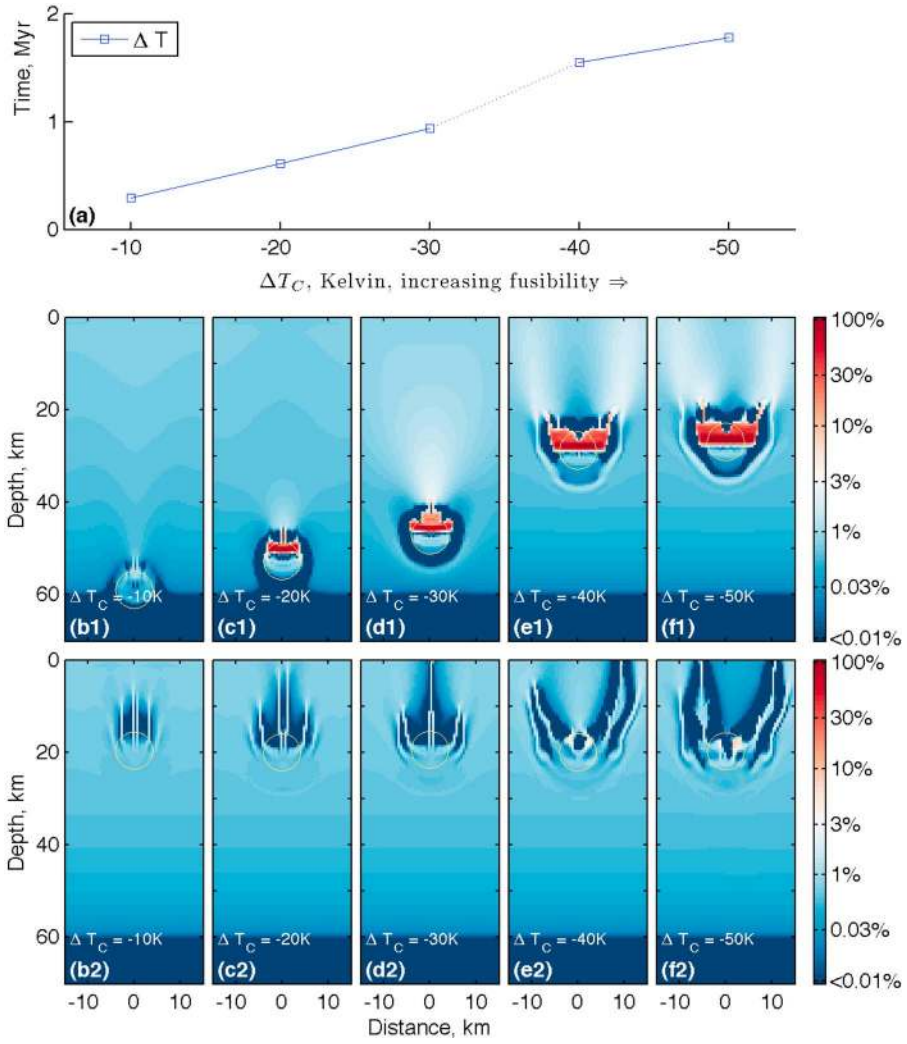

Figure 7. Solutions to a suite of five different experiments for which the enrichment of the heterogeneity ΔT_C is varied. All other parameters use the default values given in Table 1. (a) This panel shows how the time Δt between the onset of channelization and the onset of melting within the enclave varies with ΔT_C. The dotted line indicates where the relationship between Δt and ΔT_C is uncertain. (b1–f2) These panels show solutions from each experiment, in terms of porosity at the instant preceding channelization. (b2–f2) These panels show the solutions in terms of porosity at $t = 2.01$ Myr. Snapshots referenced by the same letter are taken from the same experiment. Yellow circles show what would be the perimeter of the unmolten enclave.

melting rate within an enclave varies with its size. However, *Katz and Rudge* [2011] relate the degree of melting to a Peclet number for the enclave, which represents the balance between diffusion-driven and adiabatic melting, and show that the melting rate decreases with increasing radius of the enclave. Since larger enclaves also contain a greater mass of the more fusible component, they can supply channels with enriched magma for a longer period of time. In consequence, their channels are more enriched and grow to greater lengths via reactive flow (Figure 6). Characteristics of more fertile channels include a higher melting rate, larger porosity, and a greater flux of magma.

3.3.2. Fertility

[44] Figure 7 examines the effect of the enclave's fertility on channelization through another suite of five experiments. The enclave in each experiment takes a different initial ΔT_C, and the values of all other parameters are held constant at the values listed in Table 1.

[45] Figure 7a illustrates the principal trend that emerges from this suite of experiments. It shows that the difference in time between the onset of channelization and the onset of melting within the enclave, Δt, is negatively correlated with ΔT_C. Rather than describe the data with a single line,

we tentatively suggest that the data lie on two branches. The first branch describes the data for $\Delta T_C \geq -30$ K, and the second branch spans the data for $\Delta T_C \leq -40$K. To better understand this trend we refer to the snapshots from each experiment that are shown in Figures 7b1–7f2.

[46] Figures 7b1–7f1 show porosity fields at the onset of channelization. These figures show that more fusible heterogeneities begin to channelize at shallower depths. The figures also show a cool diffusion halo surrounding each enclave. The temperature gradient across the diffusion halos is steeper for more fusible enclaves. For material within the halo to melt, the more fusible enclaves need to upwell to shallower depths. It is only when a permeable pathway connects the enclave to the ambient melting region that a channel can begin to form.

[47] Branching of the data shown in Figure 7a is a consequence of the partially molten enclave's morphology. The heterogeneities shown in Figures 7e1 and 7f1 are each associated with two large pockets of melt. These pockets lie outside the perimeter of the original heterogeneity and are formed by partial melting of the surrounding mantle rock. This consumes latent heat and establishes a diffusive heat flux into the pocket, further chilling the surrounding mantle and delaying the onset of channelization.

[48] From Figures 7b1–7f1 it is clear that more fusible enclaves produce a larger volume of magma prior to channelization. In Figures 7b2–7f2, we show the same experiments at a later model time of 2 Myr to illustrate how these different volumes of magma affect channelization. They show that the enclaves for which the initial $\Delta T_C \geq -30$°C give rise to channels with a relatively simple geometry (Figures 7b2–7d2), whereas the channels in Figures 7e2–7f2 are considerably more complex. By analyzing the full time series of results for each of the experiments, more trends emerge: channels rooted at more fertile enclaves are more enriched, accommodate higher porosities and faster fluid velocities, grow more quickly, and melt at a greater rate. However, our results suggest that no simple relationship exists between the melting rate within channels and the initial composition of the heterogeneity.

3.3.3. Upwelling Rate

[49] Figure 8 shows results from a suite of five experiments that investigate the effect of the upwelling rate W_0 on the system. For these experiments W_0 ranges from 2 cm/yr to 6 cm/yr, and all other parameters take their values from Table 1.

[50] Figure 8 shows results from the ensemble of experiments at 0.5 Myr after the onset of channelization. In general, the figures show a subtle increase in the melting rate with W_0 for the ambient melting region. Correspondingly, the magma speed and porosity in the ambient melting region also increases with W_0. Figure 8 shows that spatial variations in the melting rate correlate with spatial variations in the porosity and magma speed (Figures 8a2–8e3). This is an important result that we wish to emphasize. The melting rate is large in regions where the porosity and magma speed are also large. A similar result was found by *Hewitt* [2010], who showed that the melting rate depends on the average upwelling rate $\left(\phi \mathbf{v}_f + (1-\phi)\mathbf{v}_m\right) \cdot \hat{\mathbf{k}}$.

[51] In general, the results in Figure 8 show that the upwelling rate affects the dynamics of the system principally through the melting rate. They suggest that when W_0 is large, channels evolve more quickly to develop large porosities and melting rates. However, our experiments show no clear relationship between the upwelling rate and the geometry of channels.

3.4. Shape

[52] Above we investigated the relationship between channelization and heterogeneity by considering only circular shaped compositional anomalies. Since we aim to understand the most fundamental ways in which mantle heterogeneity influences magmatic flow, this simplified approach is justified. However, there is little doubt that heterogeneities in the real mantle have a geometry that is much more complex. In the real Earth, mantle flow will fold, stretch, and thin enclaves of recycled oceanic crust [*Allègre et al.*, 1984]. Some of the enclaves will be boudinaged, and dissolution will blur the edges of enclaves.

[53] To explore whether the general behavior of our experiments holds for enclaves of different shapes, we initialized two experiments with ellipse-shaped enclaves (Figure 9). In one of the experiments (Figures 9a1 and 9a2), the ellipse is aligned with its long axis parallel to the vertical; in the other, the long axis is rotated anticlockwise from the vertical by 45°.

[54] Figures 9a1 and 9b1 show that, in contrast to the previous experiments, for which the initial shape of the enclave was circular, the pocket of magma can be wider than the enclave. Figures 9a2

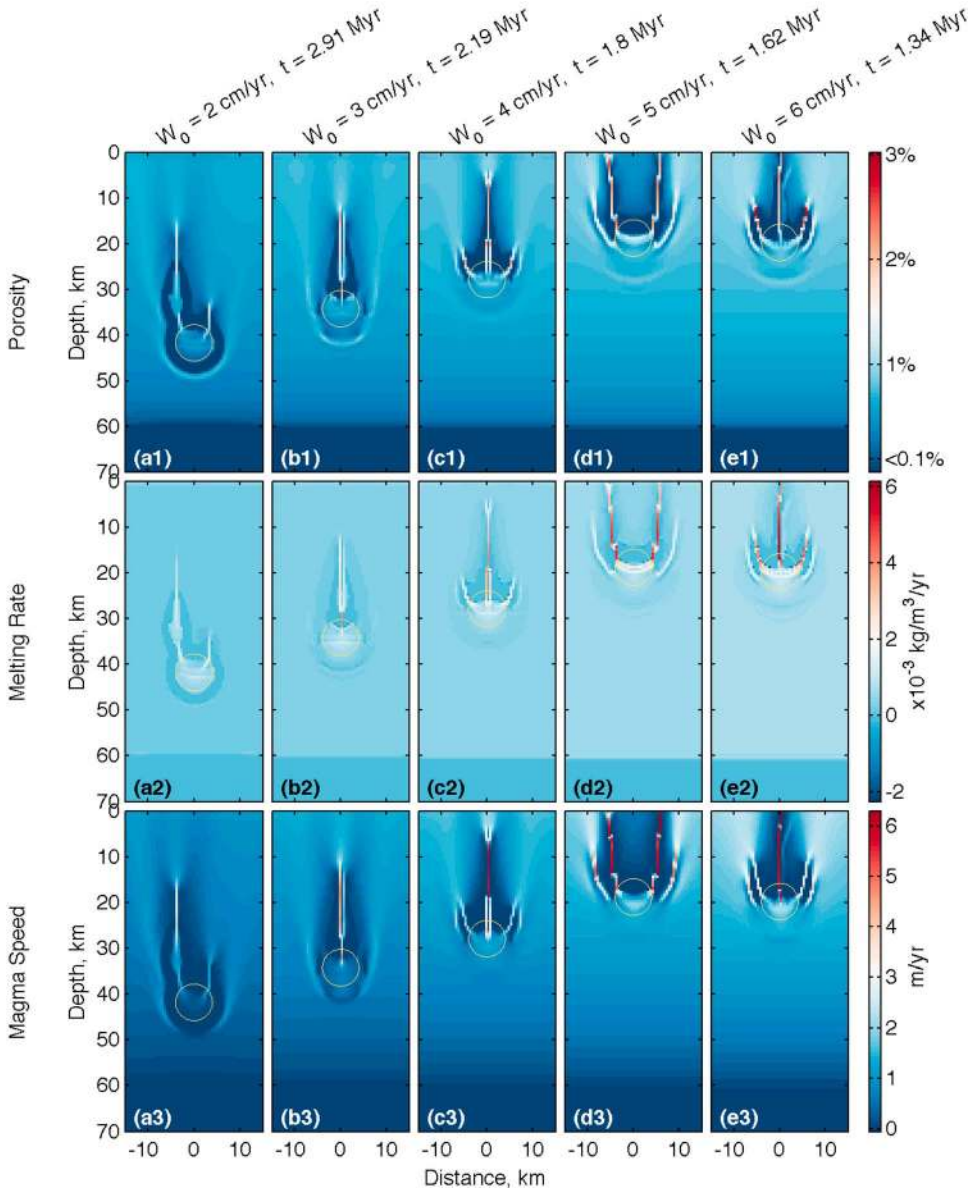

Figure 8. Solutions to a suite of five different experiments for which the upwelling rate is varied. All other parameters take the values given in Table 1. Figures show snapshots from the experiment at 0.5 Myr after the onset of channelization. Snapshots referenced by the same letter are taken from the same experiment. (a1–e1) These panels show the solutions in terms of porosity. (a2–e2) These panels show them in terms of the melting rate. (a3–e3) These panels show the solutions in terms of the magma speed. Yellow circles show what would be the perimeter of the unmolten enclave.

and 9b2 show that the ellipse-shaped enclaves also produce channels. The geometry of these channels is arguably more complex than in the previous simulations. To illustrate, the enclave in Figure 9a2 hosts two widely spaced channels that are growing in synchrony, and in Figure 9b2, the large channel incorporates lateral deviations along its length. Nevertheless, the basic behavior of the channels and their relationship with the surrounding mantle is consistent with the experiments described in the previous sections.

3.5. Summary of Numerical Results

[55] We investigated how the dynamics of magmatic channelization varies in response to changes in latent heat L, thermal diffusivity κ, the size R, shape, the fusibility of the heterogeneity, and the upwelling rate of the mantle W_0. Our numerical

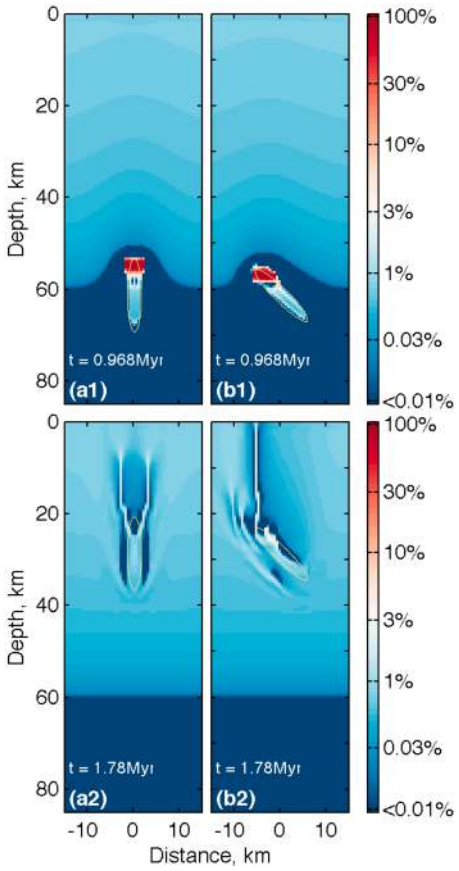

Figure 9. Solutions to two different experiments shown in terms of porosity. The original shape of the enclave for both experiments is an ellipse. The ellipse shown in Figures 9b1 and 9b2 has been rotated by 45°. The long and short axes of the ellipse are in km. All other parameters take the default values given in Table 1. Snapshots referenced by the same letter are taken from the same experiment. Yellow ellipses show what would be the perimeter of the unmolten enclaves.

experiments indicate that the evolution of high-porosity channels is coupled to composition, heat flow, and fluid dynamics of the system. To summarize, channels grow faster, and are depleted more rapidly when L is small and κ is large. Fast-growing channels tend to have higher porosities, faster magma speeds, and greater melting rates. These properties are also apparent in channels that evolve in systems where the heterogeneities are larger and more fusible (ΔT_C is more negative), and the upwelling rate is faster.

[56] Many of the trends apparent in each of the suites of experiments above are best understood in terms of the melting rate. We showed that melting rate Γ depends on a range of thermodynamic and geophysical parameters. Specifically, the melting rate increases with the upwelling rate (Figure 8), magma speed (Figures 3 and 8), porosity (Figures 3 and 8), and the thermal diffusivity (Figure 5). They also show, in Figure 4, that Γ scales inversely with L. In the next section we quantify the effect that the upwelling rate, thermal diffusivity, latent heat and composition have on the melting rate, and explore the processes that give rise to spatial variations of Γ.

4. Discussion

4.1. Melting Rate

[57] The governing equations ((A1)–(A4)) can be combined to give a thermodynamically consistent expression for the melting rate. The derivation is presented in Appendix B; here we emphasize the most important findings. For a diffusive system that is not necessarily in steady state, and for which $M_S = M_L = M$, the melting rate is

$$\Gamma = \mathcal{G}\left[\mathcal{A}\bar{\mathbf{v}} \cdot \mathbf{k} + \kappa\nabla^2 T - M\mathcal{D}\nabla \cdot \phi\nabla C_f\right], \tag{5}$$

where $\mathcal{G}$ and $\mathcal{A}$ are dimensional constants

$$\mathcal{G} = \frac{\rho}{L/c_P + \Delta CM}, \tag{6}$$

$$\mathcal{A} = \left(\frac{\rho g}{\gamma} - \frac{\alpha\mathcal{T}g}{c_P}\right). \tag{7}$$

Equation (5) shows that the melting rate is a constant multiple of contributions from the phase averaged upwelling rate, thermal diffusion, and chemical diffusion in the liquid phase. The multiplying constant $\mathcal{G}$ (equation (6)) depends on the reference density ρ, the ratio of the latent heat of fusion and the specific heat capacity, and ΔCM, which is the temperature difference between the solidus and liquidus at a fixed composition. Using values from Table 1, $(L/c_P)/(\Delta CM) \approx 10$. As such, the multiplying constant $\mathcal{G}$ depends more strongly on the ratio of the latent heat of fusion and the specific heat capacity than on properties of the phase diagram. Furthermore, L determines how strongly the melting rate is coupled to the energetics of the system. Taking $L \rightarrow 0$ removes the principal coupling between the melting rate and the energetics of the system. In this case, our expression for the melting rate is similar to that for the reactive flow models of *Liang et al.* [2010] and *Schiemenz et al.* [2011], who neglect conservation of energy.

[58] The first term in equation (5) shows that Γ depends on a constant multiple of the phase averaged upwelling rate. Because Γ depends on, and increases

with, the upwelling rate of the magma, our expression for the melting rate (equation (5)) models reactive flow. Unlike the other two terms in equation (5), $\bar{\mathbf{v}}$ is prefactored by an additional constant $\mathcal{A}$. The constant $\mathcal{A}$ depends on the Clapeyron slope and incorporates a small correction for adiabatic cooling. The product of these constants is closely related to standard expressions for the productivity $\mathcal{GA} = -\frac{\partial F}{\partial p}$ [*Asimow et al.*, 1997; *McKenzie*, 1984]. The first term in equation (5) is identical to the melting rate derived by *Hewitt* [2010], who solved similar governing equations but neglected diffusion. He derived an approximate stability condition for the melting rate and found that the thermodynamically consistent mechanism that drives the reactive infiltration instability is a melting rate that increases with the melt flux. The increase in porosity caused by the melt flux is countered by compaction, but the rate of compaction also increases with the melt fraction. For this reason, compaction tends to stabilize small perturbations. In the non-diffusive case *Hewitt* [2010] found that the system is unstable only if the rate of porosity generation by melting exceeds the rate of destruction by compaction.

[59] The second and third terms in equation (5) demonstrate that the melting rate depends on thermal and chemical diffusion in the magma. They show that heat diffuses into partially molten, enriched heterogeneities and increases the melting rate, whereas chemical diffusion blurs compositional gradients and reduces the melting rate. Using the nondimensional quantities outlined in Appendix A, the second term in equation (5) for thermal diffusion scales as $\kappa\delta T/l^2$, where l is a diffusive length scale, and the third term in equation (5) for chemical diffusion scales as $\mathcal{D}M\delta C/l^2$. Since $\delta T = M\delta C$, the relative size of these scales is $\kappa \gg \mathcal{D}$. In other words, the contribution to the melting rate from chemical diffusion relative to that from thermal diffusion is negligible.

[60] Given this scaling, we neglect chemical diffusion and rewrite the melting rate as

$$\Gamma \approx \mathcal{G}\left[\mathcal{A}\bar{\mathbf{v}} \cdot \mathbf{k} + \kappa\nabla^2 T\right]. \tag{8}$$

Equation (8) emphasizes that thermal diffusion powers melting in cooler regions. Since the assumption of thermodynamic equilibrium explicitly relates temperature and composition, the melting rate can be re-expressed in terms of C_f by combining equations (4) for the linearized liquidus and (8) to give

$$\Gamma = \mathcal{G}\left[\mathcal{A}\bar{\mathbf{v}} \cdot \mathbf{k} + \kappa M\nabla^2 C_f\right]. \tag{9}$$

Equation (9) shows that compositional variation gives rise to spatial variations in the melting rate. Importantly, though, the dependency of the melting rate on the second derivative of composition is through the thermal diffusivity. Equation (9) also implies that the melting rate within channels is related to the composition of the heterogeneity at which it is rooted. However, this relationship is not straightforward, since the prior reaction history will have modified the composition of magma and rock at any point in a channel. The composition of the magma will be further modified by melts that are drawn into the channel from the ambient mantle.

[61] From equations (8) and (9) it is clear that the melting rate depends on several different variables. To better understand these dependencies, we decompose the melting rate into three terms:

$$\Gamma = \Gamma_W + \Gamma_R + \Gamma_T. \tag{10}$$

Here, $\Gamma_W = \mathcal{GA}\mathbf{v}_m \cdot \mathbf{k}$ is the contribution from the matrix velocity, $\Gamma_R = \mathcal{GA}\phi\left(\mathbf{v}_f - \mathbf{v}_m\right)\cdot\mathbf{k}$ is the contribution to the melting rate from reactive flow, and $\Gamma_T = \mathcal{G}\kappa\nabla^2 T$ is the contribution from thermal diffusion.

[62] To determine the relative importance of each of the terms in equation (10), we applied the decomposition to the representative calculation presented in Figure 3. Figure 10 shows the contributions from Γ_W, Γ_R, and Γ_T, expressed as a fraction of Γ. Figures 10b–10d show that in the ambient melting region, at distances far from the enclave and channel network, decompression accounts for the majority of the total melting rate. At the base of the ambient melting region, Γ_W accounts for over 95% of the total melting rate. The ambient porosity and the magma speed increase toward the surface. Consequently Γ_W/Γ decreases and the contribution from reactive flow, Γ_R, becomes more important. Close to the top of the ambient melting region, Γ_W accounts for approximately 80% of the total ambient melting rate, Γ_R supplies the remaining 20%, and the contribution from thermal diffusion is negligible.

[63] Within the fertile enclave Γ_W and Γ_T each account for approximately 45% of the total melting rate, while Γ_R supplies the remaining 10%. These results show that diffusion of heat into a fertile enclave increases melting by a factor of 2 over that from adiabatic upwelling. Figure 10d shows that thermal diffusion suppresses melting in the mantle that surrounds the heterogeneity to values lower than that for the ambient mantle at equal depths.

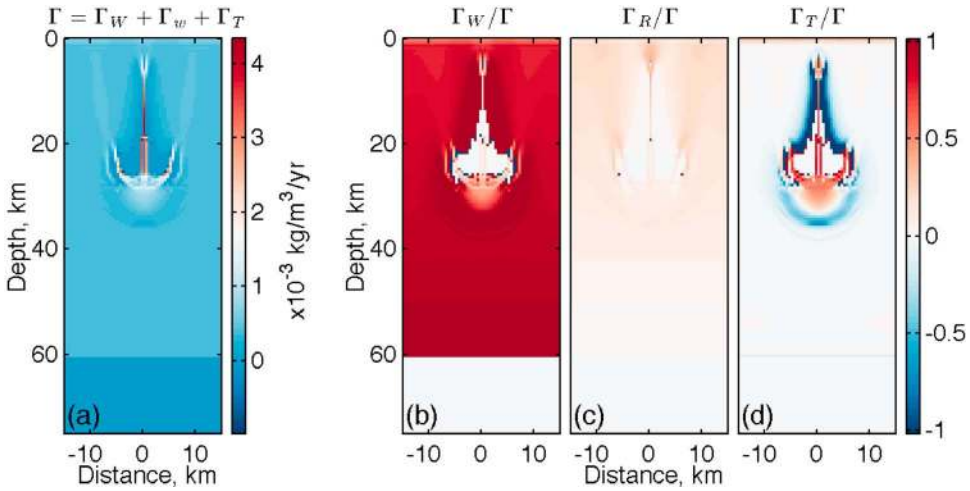

Figure 10. (a) A solution in terms of the melting rate from an experiment run with the default parameter values (Table 1) after a model time of 1.81 Myr. The melting rate is the sum of contributions from the upwelling rate of the matrix Γ_W, the upwelling rate of the magma Γ_R, and thermal diffusion Γ_T. (b–d) Contributions to the melting rate from Γ_W, Γ_R and Γ_T respectively, each expressed as a fraction of the total melting rate.

The positive contributions to melting, therefore, are decompression and reactive flow in the approximate ratio 10:1.

[64] Figure 10a shows that the greatest melting rates occur within the channel. The characteristic features of channels that give rise to large melting rates are large porosities, fast magma speeds, and a discrete, steep-sided composition anomaly across which the $\nabla^2 C_f$ is large and positive. Figures 10b–10d show that thermal diffusion provides the most significant contribution to the melting rate within channels. In this case, Γ_T accounts for approximately 60% of the total melting rate within the channel, Γ_R accounts for approximately 30%, and Γ_W supplies the remaining 10%. Thermal diffusion, therefore, powers much of the melting within channels. But in the surrounding mantle, it suppresses melting to such an extent that the $\Gamma < 0.2\Gamma_W$.

[65] The results in Figure 10 show that the relative importance of Γ_W, Γ_R, and Γ_T to the melting rate varies with the flow regime. In the ambient melting region where magmatic flow is in steady state, the decompression rate of the matrix provides the most important contribution to the melting rate. In regions where magmatic flow is channelized, thermal diffusion provides the greatest contribution to the melting rate; reactive flow accounts for much of the remainder.

4.2. Limitations of the Model

[66] Results presented in this paper indicate that magmatic channelization is a consequence of melting in a chemically heterogeneous mantle. The model is necessarily simplified in order to address the fundamental dynamics of the system. An important assumption made by the model is that local thermodynamic equilibrium holds everywhere. Estimates for the Damköhler number of the mantle, which measures the relative importance of advection and reaction, are, in general, poorly constrained [*Aharonov et al.*, 1995; *Spiegelman et al.*, 2001; *Spiegleman and Kelemen*, 2003], but are large enough for thermodynamic equilibrium to be a judicious approximation.

[67] Another important assumption inherent in the petrological model is that melting is congruent throughout the top 100 km of the mantle. *Chen and Presnall* [1975], however, showed that in the pressure range spanned by the melting region beneath mid-ocean ridges, the mode of orthopyroxene melting switches from congruent at high pressure to incongruent at low pressure. Since incongruent melting replaces fusible orthopyroxene with inert olivine, the melting rate in dunite channels will be lower than congruently melting channels under similar conditions.

[68] In general, the nature of mantle heterogeneity is poorly constrained. Almost certainly, heterogeneities occur across a range of length-scales with a variety of fusibilities and complex topologies. Using the same model as presented in this paper, *Katz and Weatherley* [2012] suggest that kilometer-scale heterogeneities of relatively low fusibility ($\Delta T_C \approx -5$K) are capable of nucleating magmatic channels. However, to investigate how the system

responds to heterogeneities on a sub-kilometer scale requires more challenging simulations at higher resolution.

[69] A persistent feature of the experiments reported here is that magmatic channels evolve to be just one grid cell wide. Grid scale features seem to be a hallmark of existing numerical experiments that use the Enthalpy Method. *Hewitt* [2010] found similar behavior in his calculations of magma flow in the mantle, as did *Katz and Worster* [2008] in their calculations of chimney formation in mushy layers. These features may stem from the numerical methods adopted by these studies. Given this, the reason for grid scale channels may be that the fluid pressure, at any constant depth, is lowest in the center of a channel, and melt consequently moves toward the grid cell that corresponds to the center of the channel. Irrespective of the resolution, magma always appears to localize to this central cell. Only if the porosity there reached 100% would we expect the channel to occupy a wider space. In this limit, however, magma flow cannot be described by Darcy's law, and the study would require a different parameterization, such as that used by *Hewitt and Fowler* [2009].

[70] Alternatively, higher-order numerical methods, such as those used by *Liang et al.* [2011] and *Hesse et al.* [2011], may improve the resolution of channels, and resolve further instabilities in the system. For example, *Richter and Daly* [1989] suggested that melting in a heterogeneous mantle will give rise to porosity waves. *Liang et al.* [2011] and *Hesse et al.* [2011] verified this and showed that nonlinear interactions between compaction and dissolution give rise to porosity waves and magmatic channels. Their results offer an additional mode of channel formation, but it remains to be shown that these additional instabilities feature in systems that conserve energy.

5. Conclusions

[71] Results from our energetically consistent model of magma flow and congruent melting indicate that channelized melt transport is a consequence of melting in a heterogeneous mantle. Channels arise when magma from partially molten heterogeneities supplies the ambient mantle with an additional, and sufficient, flux of magma. The results are best understood in light of the melting rate, which is derived from conservation principles. The melting rate is coupled to the energetic budget dominantly through the latent heat. For values close to the estimated latent heat of the mantle, the mode of melt transport in the absence of heterogeneities is diffuse porous flow. Selecting a small value for the latent heat decouples the melting rate from the energetic budget; under these conditions, the model of melt transport in a chemically homogeneous mantle is channelized flow.

[72] The melting rate is a linear combination of contributions from decompression, reactive flow, and thermal diffusion. In the ambient melting region (i.e. not within, or in the vicinity of, high-porosity channels), melting is largely the response of adiabatic decompression. Within channels, however, thermal diffusion provides the most significant contribution to the melting rate. Since heat diffuses into channels, the adjacent mantle is starved of energy for melting. The permeability of these rocks is low, and magma upwelling from deeper depths is focused into high-porosity regions. Consequently, thermal diffusion provides a positive feedback on channelization, and could discourage mixing between magmas flowing through channels and magmas in the adjacent mantle. Our results predict, for the first time, that thermal diffusion is important to the genesis and dynamics of magmatic channels, and underscore the need to use energetically consistent models in studies of coupled magma/mantle dynamics.

Appendix A: Governing Equations

[73] The models used in this paper are based on conservation statements for mass and momentum for the solid rock and liquid magma, conservation of chemical composition within those phases, and conservation of energy. These statements, first derived by *McKenzie* [1984], were reformulated by *Katz et al.* [2007] to make them more amenable to numerical solution. *Katz* [2010] provides a comprehensive derivation of the equations for conservation of energy and composition. In this study, the equations that govern the mechanics of the system are simplified, in that matrix shear is neglected and the fluids are assumed to be Boussinesq. The set of partial differential equations that we use to model the coupled dynamics of magma and mantle rock are

$$-\nabla\cdot\frac{K}{\mu}\nabla\mathcal{P}+\frac{\mathcal{P}}{\xi}=\nabla\cdot\frac{K}{\mu}(1-\phi)\Delta\rho\mathbf{g}, \tag{A1}$$

$$\frac{\mathcal{P}}{\xi}=\nabla^2 U, \tag{A2}$$

$$\frac{\partial \mathcal{H}}{\partial t} + \rho c_P \mathcal{T} e^{\frac{\alpha g z}{c_P}} \bar{\mathbf{v}} \cdot \nabla \mathcal{T} = L[\rho \nabla \cdot (1-\phi)\mathbf{v}_m] + k e^{\frac{\alpha g z}{c_P}} \nabla^2 \mathcal{T}, \tag{A3}$$

$$\frac{\partial C}{\partial t} + \nabla \cdot \phi \mathbf{v}_f C_f + \nabla \cdot (1-\phi)\mathbf{v}_m C_m = \mathcal{D} \nabla \cdot \phi \nabla C_f. \tag{A4}$$

Equations (A1) and (A2) conserve mass and momentum for the mantle rock and magma. Here, K is the permeability, and is related to the porosity ϕ by

$$K = k_0 \phi^3, \tag{A5}$$

where k_0 is a reference permeability. μ is the viscosity of the magma, and $\xi = \zeta + 4/3\eta_0$, where ζ is the bulk viscosity and η_0 is the reference shear viscosity. We define $\zeta = \eta_0/\phi$, in agreement with *Simpson et al.* [2010]. $\Delta\rho$ is the difference in density between solid rock and magma, and $\mathbf{g}$ is gravity. $\mathcal{P}$ is the pressure that the matrix exerts on the magma when rock compacts, and $\nabla U = \mathbf{v}_m$ describes the matrix velocity $\mathbf{v}_m$ in terms of a compaction potential U. We solve equations (A1) and (A2) for $\mathcal{P}$ and U respectively.

[74] Equation (A3) relates temporal changes in enthalpy to advection of latent heat and sensible heat and diffusion of heat. In this equation, $\mathcal{H} = \rho L \phi + \rho c_P (T - T_0)$ defines the volumetric bulk enthalpy $\mathcal{H}$, where ρ is the density, L is the latent heat of fusion, c_P is the specific heat capacity, and T is temperature; T_0 is the solidus temperature at zero pressure and $C_m = C_0$. Additionally, t is time, $\mathcal{T}$ is the potential temperature of the mantle, α is the coefficient of thermal expansion for the rock, and κ is the thermal diffusivity.

[75] Equation (A4) conserves the bulk composition $C = \phi C_f + (1-\phi)C_m$, where C_f is the composition of the magma, and C_m is the composition of the solid rock. $\mathcal{D}$ is the chemical diffusivity, and $\mathbf{v}_f$ is the velocity of the magma, given by

$$\mathbf{v}_f = \mathbf{v}_m - \frac{K}{\mu\phi}\left[\nabla P_f - \rho \mathbf{g}\right], \tag{A6}$$

[*McKenzie*, 1984], where P_f is the fluid pressure.

A1. Boundary Conditions

[76] The boundary conditions for material flowing into the domain (Figure 1, bottom boundary) are as follows:

$$\mathcal{H} = \rho c_P \exp\left(\frac{\alpha g z_b}{c_P}\right)(\mathcal{T} + T_0) - \rho c_P T_0, \tag{A7}$$

$$C = C_0, \tag{A8}$$

$$\frac{\partial U}{\partial z} = W_0, \tag{A9}$$

$$\mathcal{P} = 0. \tag{A10}$$

They specify that solid rock flows into the domain at a rate W_0 (equation (A9)). It has a bulk composition C_0, and a total enthalpy given by equation (A7), where z_b is the depth of the bottom boundary. Since the rock is solid the compaction pressure is zero (equation (A10)).

[77] The outflow boundary conditions (Figure 1, top boundary) are designed to allow material to flow unrestrictedly out of the domain. We impose $\partial\phi/\partial z = 0$ and $\partial\mathcal{T}/\partial z = 0$, then specify

$$\mathcal{H} = \rho L \phi + \rho c_P \exp\left(\frac{\alpha g z_t}{c_P}\right)(\mathcal{T} + T_0) - \rho c_P T_0, \tag{A11}$$

$$\frac{\partial C}{\partial z} = 0, \tag{A12}$$

$$U = 0, \tag{A13}$$

$$\frac{\partial \mathcal{P}}{\partial z} = 0. \tag{A14}$$

These conditions prescribe the vertical derivatives of C, U, and $\mathcal{P}$ to be zero on the boundary. The enthalpy of the outflowing material is given by equation (A11), where z_t is the depth of the boundary.

A2. Nondimensionalization

[78] The following characteristic scales are used to nondimensionalize the governing equations ((A1)–(A4))

$$\begin{gathered} \mathbf{x} = H\mathbf{x}', \quad \mathbf{v} = w_0 \mathbf{v}', \\ t = \frac{H}{w_0} t', \quad K = k_0 K', \\ \mathcal{P} = H\Delta\rho g \mathcal{P}' \quad \mathcal{H} = \rho c_p \Delta T \mathcal{H}', \\ \Gamma = \frac{w_0 \rho}{H}\Gamma', \quad w_0 = \frac{k_0 \Delta\rho g}{\mu}, \\ (\eta, \varsigma, \xi) = \eta_0(\eta', \varsigma', \xi') \end{gathered} \tag{A15}$$

where H is the height of the domain, and $w_0 = k_0\Delta\rho g/\mu$ is the reference magma velocity. To nondimensionalize temperature and composition, we use the following variables

$$\theta = \frac{\mathcal{T} - T_0}{\Delta T}, \quad \bar{\theta} = \frac{T - T_0}{\Delta t}, \quad \Theta = \frac{C - C_0}{\Delta C}. \tag{A16}$$

Substituting these quantities into equations (A1)–(A4) and dropping the primes yields

$$-\nabla \cdot K\nabla \mathcal{P} + \frac{H^2}{\delta^2}\frac{\mathcal{P}}{\xi} = \nabla \cdot (1-\phi)\hat{\mathbf{k}}, \tag{A17}$$

$$\frac{H^2}{\delta^2}\frac{\mathcal{P}}{\xi} = \nabla^2 U, \tag{A18}$$

$$\frac{\partial \mathcal{H}}{\partial t} + e^{\mathcal{A}z}\bar{\mathbf{v}} \cdot \nabla\theta = \mathcal{S}\nabla \cdot (1-\phi)\mathbf{v}_m + \mathrm{Pe}_T^{-1} e^{\mathcal{A}z}\nabla^2\theta, \tag{A19}$$

$$\frac{\partial \Theta}{\partial t} + \nabla \cdot \phi\mathbf{v}_f\Theta_f + \nabla \cdot (1-\phi)\mathbf{v}_m\Theta_m = \mathrm{Pe}_C^{-1}\nabla \cdot \phi\nabla\Theta_f, \tag{A20}$$

where $\delta = \sqrt{\eta_0 k_0/\mu}$ is the compaction length, the Stefan number $\mathcal{S} = L/c_p\Delta T$, $\mathcal{A} = \alpha g H/c_P$ is the adiabatic constant, and $\mathrm{Pe}_T = Hw_0/\kappa$ and $\mathrm{Pe}_C = Hw_0/\mathcal{D}$ are the thermal and chemical Peclet numbers respectively.

Appendix B: Melting Rate

[79] The melting rate is derived by combining conservation statements for energy (equation (1)) and composition (equation (2)) with equations that conserve mass for the liquid and solid phases. The equations for conservation of mass are

$$\frac{\partial \phi}{\partial t} + \nabla \cdot \phi\mathbf{v}_f = \frac{\Gamma}{\rho}, \tag{B1}$$

$$\frac{\partial (1-\phi)}{\partial t} + \nabla \cdot (1-\phi)\mathbf{v}_m = -\frac{\Gamma}{\rho}. \tag{B2}$$

For this derivation, we express the equation for conservation of energy in terms of the actual temperature, rather than the potential temperature. With this modification, the conservation of energy is

$$\frac{\partial \mathcal{H}}{\partial t} - \rho L\nabla \cdot (1-\phi)\mathbf{v}_m + \rho c_P\bar{\mathbf{v}}\nabla T - \rho\alpha T\mathbf{g} \cdot \bar{\mathbf{v}} = k\nabla^2 T, \tag{B3}$$

where k is the thermal conductivity.

[80] We combine equations (2) and (B3) with equations (B1) and (B2), and substitute in the definition $\mathcal{H} = \rho L\phi + \rho c_P(T - T_0)$ to express the statements conserving energy and composition in terms of the melting rate Γ:

$$L\Gamma + \rho c_P\frac{\partial T}{\partial t} + \rho c_P\bar{\mathbf{v}} \cdot \nabla T - \rho\alpha\mathcal{T}_0\mathbf{g} \cdot \bar{\mathbf{v}} = k\nabla^2 T, \tag{B4}$$

$$\frac{\Gamma}{\rho}(C_f - C_m) + \phi\frac{\partial C_f}{\partial t} + \phi\mathbf{v}_f \cdot \nabla C_f + (1-\phi)\frac{\partial C_m}{\partial t} + (1-\phi)\mathbf{v}_m \cdot \nabla C_m = \mathcal{D}\nabla \cdot \phi\nabla C_f, \tag{B5}$$

where we have simplified the adiabatic term by taking $T = \mathcal{T}_0$. Next, we use equations (3) and (4) to rewrite equation (B4) in terms of C_f, and to eliminate C_m from equation (B5) . By making these modifications and combining the results, the melting rate is given by

$$\Gamma = \mathcal{G}\mathcal{B}\left[\frac{\alpha\mathcal{T}}{c_p} - \frac{\rho}{\gamma}\right] + \mathcal{G}\left(\phi\mathbf{v}_f + \frac{(1-\phi)}{R}\mathbf{v}_m\right) \cdot \nabla C_f M_l - \mathcal{G}\mathcal{B}\bar{\mathbf{v}} \cdot \nabla T + \mathcal{G}\mathcal{B}\kappa\nabla^2 T - \mathcal{G}\mathcal{D}\nabla \cdot \phi\nabla C_f M_L, \tag{B6}$$

where

$$\mathcal{G} = \frac{\rho}{L/c_p[\phi(1-1/R)+1/R] + \Delta C M_L - M_L(C_f - C_0)(1-1/R)}, \tag{B7}$$

$$R = \frac{M_S}{M_L}, \tag{B8}$$

and

$$\mathcal{B} = \frac{\phi(R-1)+1}{R}. \tag{B9}$$

To arrive at the expression for the melting rate given by equation (5), we take $R = 1$, which renders $\mathcal{B} = 1$, and $\mathcal{G} = \rho/(L/c_P + \Delta C M)$.

Acknowledgments

[81] We would like to thank Ian Hewitt for useful discussions that improved this manuscript, Yan Liang and Dave Stevenson for their helpful and constructive reviews, and Joel Baker for handling the manuscript. We gratefully acknowledge Oxford Supercomputing Centre for providing compute time, HPC resources, and technical support.

References

Aharonov, E., J. A. Whitehead, P. B. Kelemen, and M. Spiegelman (1995), Channeling instability of upwelling melt in the mantle, *J. Geophys. Res.*, *100*, 20,433–20,450.

Aharonov, E., M. Spiegelman, and P. Kelemen (1997), Three-dimensional flow and reaction in porous media: Implication for the Earth's mantle and sedimentary basins, *J. Geophys. Res.*, *102*, 14,821–14,883.

Alabaster, T., J. A. Pearce, and J. Malpas (1982), The volcanic stratigraphy and petrogenesis of the Oman ophiolite complex, *Contrib. Mineral. Petrol.*, *81*, 168–183.

Alexiades, V. and A. D. Solomon (1993), *Mathematical Modeling of Melting and Freezing Processes*, Hemisphere, Washington, D. C.

Allègre, C., and D. L. Turcotte (1986), Implications of a 2-component marble-cake mantle, *Nature*, *323*(6084), 123–127.

Allègre, C., B. Hamelin, and B. Dupré (1984) Statistical analysis of isotopic ratios in MORB: The mantle blob cluster model and the convective regime of the mantle, *Earth Planet. Sci. Lett.*, *71*, 71–84.

Asimow, P. D., M. M. Hirschmann, and E. M. Stolper (1997), An analysis of variations in isentropic melt productivity, *Philos. Trans. R. Soc. London A*, *355*, 255–281.

Balay, S., W. D. Gropp, L. Curfman McInnes, and B. F. Smith (1997), Efficient management of parallelism in object oriented numerical software libraries, in *Modern Software Tools in Scientific Computing*, edited by E. Arge, A. M. Bruaset, and H. P. Langtangen, pp. 163–202, Birkhauser, Boston, Mass.

Balay, S., K. Buschelman, V. Eijkhout, W. D. Gropp, D. Kaushik, M. G. Knepley, L. Curfman McInnes, B. F. Smith, and H. Zhang (2009), PETSc users manual, 3.0.0 revision, *Tech. Rep. ANL-95/11*, Argonne Natl. Lab., Argonne, Ill. [Available at http://www.mcs.anl.gov/petsc/petsc-3.0.0/docs/manual.pdf.]

Ben Othman, D., and C. J. Allegre (1990), U-Th isotopic systematics at 13°n east Pacific Ridge segment, *Earth Planet. Sci. Lett.*, *98*(1), 129–137.

Bercovici, D., Y. Ricard, and G. Schubert (2001), A two-phase model for compaction and damage: 1. General theory, *J. Geophys. Res.*, *106*, 8887–8906.

Chabaux, F., and C. J. Allègre (1994), 238U–230Th–226Ra disequilibria in volcanics: A new insight into melting conditions, *Earth Planet. Sci. Lett.*, *126*, 61–74.

Chadam, J., D. Hoff, E. Merino, P. Ortoleva, and A. Sen (1986), Reactive infiltration instabilities, *IMA J. Appl. Math.*, *36*, 207–221.

Chen, C. H., and D. C. Presnall (1975), The system Mg_2SiO_4-SiO_2 at pressures up to 25 kilobars, *Am. Mineral.*, *60*, 398–406.

Fowler, A. (1985), A mathematical model of magma transport in the asthenosphere. *Geophys. Astrophys. Fluid Dyn.*, *33*, 63–96.

Gale, A., S. Escrig, E. J. Gier, C. H. Langmuir, and S. L. Goldstein (2011), Enriched basalts at segment centers: The Lucky Strike (37°17′N) and Menez Gwen (37°50′N) segments of the Mid-Atlantic Ridge, *Geochem. Geophys. Geosyst.*, *12*, Q06016, doi:10.1029/2010GC003446.

Grove, T. L., R. J. Kinzler, and W. B. Bryan (1992), Fractionation of mid-ocean ridge basalt, in *Mantle Flow and Melt Generation at Mid-Ocean Ridges*, *Geophys. Monogr. Ser.*, vol. 71, pp. 281–310, Washington, D. C.

Hart, S. (1993), Equilibration during mantle melting: A fractal tree model, *Proc. Natl. Acad. Sci.*, *90*, 11,914–11,918.

Helffrich, G. (2002), Chemical and seismological constraints on mantle heterogeneity, *Philos. Trans. R. Soc. London A*, *360*, 2493–2505.

Hesse, M. A., A. R. Schiemenz, Y. Liang, and E. M. Parmentier (2011), Compaction-dissolution waves in an upwelling mantle column, *Geophys. J. Int.*, *187*, 1057–1075.

Hewitt, I. J. (2010), Modelling melting rates in upwelling mantle, *Earth Planet. Sci. Lett.*, *300*, 264–274.

Hewitt, I. J., and A. C. Fowler (2009), Melt channelization in ascending mantle, *J. Geophys. Res.*, *114*, B06210, doi:10.1029/2008JB006185.

Hirschmann, M. M., and E. M. Stolper (1996), A possible role for garnet pyroxenite in the origin of the "garnet signature" in MORB, *Contrib. Mineral. Petrol.*, *124*(2), 185–208.

Ito, G., and J. J. Mahoney (2005), Flow and melting of a heterogeneous mantle: 1. Method and importance to the geochemistry of ocean island and mid-ocean ridge basalts, *Earth Planet. Sci. Lett.*, *230*, 29–46.

Iwamori, H. (1993), A model for disequilibrium mantle melting incorporating melt transport by porous and channel flows, *Nature*, *366*(6457), 734–737.

Jackson, M., S. Hart, A. Saal, N. Shimizu, M. D. Jurz, J. S. Blusztajn, and A. C. Skovgaard (2008), Globally elevated titanium, tantalum, and niobium (TITAN) in ocean island basalts with high 3He/4He, *Geochem. Geophys. Geosyst.*, *9*, Q04027, doi:10.1029/2007GC001876.

Johnson, K. T. M., H. J. B. Dick, and N. Shimizu (1990), Melting in the oceanic upper mantle: An ion microprobe study of diopsides in abyssal peridotites, *J. Geophys. Res.*, *95*(B3), 2261–2678.

Jull, M., P. Kelemen, and K. Sims (2002), Consequences of diffuse and channelled porous melt migration on uranium series disequilibria, *Geochim. Cosmochim. Acta*, *66*(23), 4133–4148.

Katz, R. F. (2008), Magma dynamics with the Enthalpy Method: Benchmark solutions and magmatic focusing at mid-ocean ridges, *J. Petrol.*, *49*, 2099–2121.

Katz, R. F. (2010), Porosity-driven convection and asymmetry beneath mid-ocean ridges, *Geochem. Geophys. Geosyst.*, *11*, Q0AC07, doi:10.1029/2010GC003282.

Katz, R. F., and J. F. Rudge (2011), The energetics of melting fertile heterogeneities within the depleted mantle, *Geochem. Geophys. Geosyst.*, *12*, Q0AC16, doi:10.1029/2011GC003834.

Katz, R. F., and S. M. Weatherley (2012), Consequences of mantle heterogeneity for melt extraction at mid-ocean ridges, *Earth Planet. Sci. Lett.*, in press.

Katz, R., and M. Worster (2008), Simulations of directional solidification, thermochemical convection, and chimney formation in a Hele-Shaw cell, *J. Comput. Phys.*, *227*, 9823–9840.

Katz, R. F., M. G. Knepley, B. Smith, M. Spiegelman, and E. T. Coon (2007), Numerical simulation of geodynamics processes with the Portable Extensible Toolkit for Scientific Computation, *Phys. Earth Planet. Inter.*, *163*, 52–68.

Kelemen, P., J. A. Whitehead, E. Aharonov, and K. A. Joordahl (1995), Experiments on flow focusing in soluble porous media, with applications to melt extraction from the mantle, *J. Geophys. Res.*, *100*, 475–496.

Kelemen, P. B., G. Hirth, N. Shimizu, M. Spiegelman, and H. J. B. Dick (1997), A review of melt migration processes in the adiabatically upwelling mantle beneath oceanic spreading ridges, *Philos. Trans. R. Soc. London A*, *355*(1723), 283–318.

Kelemen, P. B., M. Braun, and G. Hirth (2000), Spatial distribution of melt conduits in the mantle beneath spreading ridges: Observations from the Ingalls and Oman ophiolites, *Geochem. Geophys. Geosyst.*, *1*(7), 1005, doi:10.1029/1999GC000012.

Klein, E. M., and C. H. Langmuir (1987), Global correlations of ocean ridge basalt chemistry with axial depth and crustal thickness, *J. Geophys. Res.*, *92*(B8), 8089–8115.

Kojitani, H., and M. Akaogi (1997), Melting enthalpies of mantle peridotite: calorimetric determinations in the system CaO-MgO-Al_2O_3-SiO_2 and application to magma generation, *Earth Planet. Sci. Lett.*, *153*, 209–222.

Kokfelt, T. F., K. Hoernle, F. Hauff, J. Fiebig, R. Werner, and D. Garbe-Schoenberg (2006), Combined trace element and Pb-Nd-Sr-O isotope evidence for recycled oceanic crust

(upper and lower) in the Iceland mantle plume, *J. Petrol.*, *47* (9), 1705–1749.

Langmuir, C. H., and J. F. Bender (1984), The geochemistry of basalts in the vicinity of transform faults– Observations and implications, *Earth Planet. Sci. Lett.*, *69*(1), 107–127.

Langmuir, C. H., J. F. Bender, A. E. Bence, G. N. Hanson, and S. R. Taylor (1977), Petrogenesis of basalts from the Famous Area–Mid-Atlantic Ridge, *Earth Planet. Sci. Lett.*, *36*(1), 133–156.

Langmuir, C. H., E. M. Klein, and T. Plank (1992), Petrological systematics of mid-ocean ridge basalts: Constraints on melt greneration beneath ocean ridges, in *Mantle Flow and Melt Generation at Mid-Ocean Ridges*, *Geophys. Monogr. Ser.*, vol. 71, pp. 183–280, Washington D. C.

Lassiter, J. C., and E. H. Hauri (1998), Osmium-isotope variations in Hawaiian lavas: Evidence for recycled oceanic lithosphere in the Hawaiian plume, *Earth Planet. Sci. Lett.*, *164*, 483–496.

Liang, Y., and Y. Guo (2003), Reactive dissolution instability driven by chemical diffusion with applications to harzburgite reactive dissolution, *Geophys. Res. Lett.*, *30*(13), 1722, doi:10.1029/2003GL017687.

Liang, Y., A. Schiemenz, M. A. Hesse, E. M. Parmentier, and J. A. Hesthaven (2010), High-porosity channels for melt migration in the mantle: Top is the dunite and bottom is the harzburgite and lherzolite, *Geophys. Res. Lett.*, *37*, L15306, doi:10.1029/2006GL026616.

Liang, Y., A. Schiemenz, M. A. Hesse, and E. M. Parmentier (2011), Waves, channels, and the preservation of chemical heterogeneities during melt migration in the mantle, *Geophys. Res. Lett.*, *38*, L20308, doi:10.1029/2011GL049034.

Maclennan, J., D. McKenzie, K. Grönvold, N. Shimizu, J. M. Eiler, and N. Kitchen (2003), Melt mixing and crystallization under Theistareykir, northeast Iceland, *Geochem. Geophys. Geosyst.*, *4*(11), 8624, doi:10.1029/2003GC000558.

McKenzie, D. (1984), The generation and compaction of partially molten rock, *J. Petrol.*, *25*(3), 713–765.

McKenzie, D., and R. K. O'Nions (1991), Partial melt distributions from inversion of rare earth element concentrations, *J. Petrol.*, *32*(5), 1020–1091.

Nicolas, A. (1986), A melt extraction model based on structural studies in mantle peridoities, *J. Petrol.*, *27*, 999–1022.

Nicolas, A. (1989), *Structures of Ophiolites and Dynamics of the Oceanic Lithosphere*, Kluwer Acad., Dordrecht, Netherlands.

O'Hara, M. J. (1965), Primary magmas and the origin of basalts, *Scott. J. Geol.*, *1*, 19–40.

Ortoleva, P., J. Chadam, E. Merino, and A. Sen (1987), Geochemical self-organisationII: The reactive-infiltration instability, *Am. J. Sci.*, *287*, 1008–1040.

Pertermann, M., and M. M. Hirschmann (2003), Partial melting experiments on a MORB-like pyroxenite between 2 and 3 GPa: Constraints on the presence of pyroxentite in basalt source regions from solidus location and melting rate, *J. Geophys. Res.*, *108*(B2), 2125, doi:10.1029/2000JB000118.

Phipps Morgan, J., and J. W. Morgan (1999), Two-stage melting and the geochemical evolution of the mantle: A recipe for mantle plum-pudding, *Earth Planet. Sci. Lett.*, *170*, 215–239.

Prinzhofer, A., E. Lewin, and C. J. Allègre (1989), Stochastic melting of the marble cake mantle: Evidence from local study of the East Pacific Rise at 12 50′N, *Earth Planet. Sci. Lett.*, *92*, 189–206.

Prytulak, J., and T. Elliott (2007), Tio2 enrichment in ocean island basalts, *Earth Planet. Sci. Lett.*, *263*, 388–403.

Renna, M. R., and R. Tribuzio (2011), Olivine-rich Troctolites from Ligurian ophiolites (Italy): Evidence for impregnation of replacive mantle conduits by MORB-type melts, *J. Petrol.*, *52*, 1763–1790.

Ribe, N. (1985), The deformation and compaction of partial molten zones, *Geophys. J. R. Astron. Soc.*, *83*, 497–501.

Richter, F. M., and S. F. Daly (1989), Dynamical and chemical effects of melting a heterogeneous source, *J. Geophys. Res.*, *94*, 12,499–12,510.

Roe, P. L. (1985), Some contributions to the modelling of discontinuous flows, in *Large-Scale Computations in Fluid Mechanics*, edited by R. L. Lee et al., pp. 163–193, Am. Math. Soc., Providence, R. I.

Salters, V., and H. J. B. Dick (2002), Mineralogy of the mid-ocean-ridge basalt source from neodymium isotopic composition of abyssal peridotites, *Nature*, *418*, 68–72.

Schiemenz, A., L. Liang, and E. M. Parmentier (2011), A high-order numerical study of reactive dissolution in an upwelling heterogeneous mantle–I. Channelization, channel lithology and channel geometry, *Geophys. J. Int.*, *186*(2), 641–664.

Scott, D. R., and D. J. Stevenson (1986), Magma ascent by porous flow, *J. Geophys. Res.*, *91*, 9283–9296.

Seyler, M., D. Brunelli, M. J. Toplis, and C. Mével (2011), Multiscale chemical heterogeneities beneath the eastern Southwest Indian Ridge (52°E–68°E): Trace element compositions of along-axis dredged peridotites, *Geochem. Geophys. Geosyst.*, *12*, Q0AC15, doi:10.1029/2011GC003585.

Shorttle, O., and J. Maclennan (2011), Compositional trends of Icelandic basalts: Implications for short-length scale lithological heterogeneity in mantle plumes, *Geochem. Geophys. Geosyst.*, *12*, Q11008, doi:10.1029/2011GC003748.

Simpson, G., M. Spiegelman, and M. I. Weinstein (2010), A multiscale model of partial melts: 1. Effective equations, *J. Geophys. Res.*, *115*, B04410, doi:10.1029/2009JB006375.

Spiegelman, M. (1993), Flow in deformable porous media 1. Simple analysis, *J. Fluid Mech.*, *247*, 17–38.

Spiegleman, M., and P. B. Kelemen (2003), Extreme chemical variability as a consequence of channelized melt transport, *Geochem. Geophys. Geosyst.*, *4*(7), 1055, doi:10.1029/2002GC000336.

Spiegelman, M., and P. Kenyon (1992), The requirements for chemical disequilibrium during magma migration, *Earth Planet. Sci. Lett.*, *109*(3–4), 611–620.

Spiegelman, M., P. Kelemen, and E. Aharonov (2001), Causes and consequences of flow organization during melt transport: The Reaction Infiltration Instability in compactible media, *J. Geophys. Res.*, *106*, 2061–2077.

Šrámek, O., Y. Ricard, and F. Dubuffet (2010), A multiphase model of core formation, *Geophys. J. Int.*, *181*, 198–220.

Stolper, E. M. (1980), A phase diagram for mid-ocean ridge basalts: Preliminary results and implications for petrogenesis, *Contrib. Mineral. Petrol.*, *74*, 13–27.

Stracke, A., and B. Bourdon (2009), The importance of melt extraction for tracing mantle heterogeneity, *Geochim. Cosmochim. Acta*, *73*, 218–238.

Stracke, A., A. Zindler, V. J. M. Salters, D. Mckenzie, J. Blichert-Toft, F. Albarède, and K. Grönvold (2003), Theistareykir revisited, *Geochem. Geophys. Geosyst.*, *4*(2), 8507, doi:10.1029/2001GC000201.

Stracke, A., A. W. Hofmann, and S. R. Hart (2005), FOZO, HIMU, and the rest of the mantle zoo, *Geochem. Geophys. Geosyst.*, *6*, Q05007, doi:10.1029/2004GC000824.

Stracke, A., B. Bourdon, and D. McKenzie (2006), Melt extraction in the Earth's mantle: Constraints from U-Th-Pa-Ra studies in oceanic basalts, *Earth Planet. Sci. Lett.*, *244*, 97–112.

Tilton, G. R., C. A. Hopson, and J. E. Wright (1981), Uranium-lead isotopic ages of the Samail ophiolite, Oman, with applications to Tethyan ocean ridge tectonics, *J. Geophys. Res.*, *91*, 9261–9276.

Turner, S., and B. Bourdon (2011), Melt transport from the mantle to the crust–Uranium-series isotopes, in *Timescales of Magmatic Processes: From Core to Atmosphere*, edited by A. Dosseto, S. Turner, and J. A. Van Orman, pp. 102–115, Wiley-Blackwell, Chichester, U. K.

Walter, M. J. (1998), Melting of garnet peridotite and the origin of komatiite and depleted lithosphere, *J. Petrol.*, *39*, 29–60.

Wood, D. (1979), A variably veined suboceanic upper mantle–Genetic significance for mid-ocean ridge basalts from geochemical evidence, *Geology*, *7*, 499–503.

Yaxley, G. M., and D. H. Green (1998), Reactions between eclogite and peridotite: Mantle refertilisation by subduction of oceanic crust, *Schweiz. Mineral. Petrogr. Mitt.*, *78*, 243–255.

Zindler, A., S. Hart, F. Frey, and S. P. Jakobsson (1979), Nd and Sr isotope ratios and rare earth element abundances in Reykjanes Peninsula basalts evidence for mantle heterogeneity beneath Iceland, *Earth Planet. Sci. Lett.*, *45*, 249–262.